Environmental Research 301 (2026) 124523

Contents lists available at ScienceDirect

Environmental Research

journal homepage: www.elsevier.com/locate/envres

Radon isotopes as tracers of climate-sensitive subsurface connectivity in Antarctic permafrost

L. Ruggiero [a,b,*], A. Sciarra [b], A. Mazzini [c,d,b], F. Florindo [b], G. Wilson [e], C. Mazzoli [f], P. Tuccimei [g], G. Galli [b], L. Tositti [h], A. Zappi [h], J. Anderson [i], L. Davidson [j], E. Benà [f], V. Olivetti [f], M.C. Tartarello [k], M. Mattia [g], F. Giagnoni [g], C. Zaccone [l,b], S. Bigi [k], R. Sassi [f], G. Ciotoli [m,b]

[a] National Research Council, Infrastructures Research Office, CNR-UIR, Roma, Italy
[b] National Institute of Geophysics and Volcanology, INGV, Roma, Italy
[c] Department of Geosciences, University of Oslo, Oslo, Norway
[d] Institute for Energy Technology (IFE), Kjeller, Norway
[e] University of Waikato, Hamilton, New Zealand
[f] Department of Geosciences, University of Padova, Padova, Italy
[g] Science Department, "Roma Tre" University, Roma, Italy
[h] Department of Chemistry "Giacomo Ciamician", University of Bologna, Bologna, Italy
[i] Lamont-Doherty Earth Observatory, Columbia University, Palisades, NY, USA
[j] Department of Geology, University of Otago, Dunedin, New Zealand
[k] Earth Science Department, "Sapienza" University of Roma, Roma, Italy
[l] Department of Biotechnology, University of Verona, Verona, Italy
[m] National Research Council, Institute of Environmental Geology and Geoengineering, CNR-IGAG, Montelibretti (Roma), Italy

ARTICLE INFO

Keywords:
Radon
Thoron
Active layer
Antarctic permafrost
Soil-gas transport
Radon exhalation
McMurdo dry valleys
RAD7

ABSTRACT

Assessing how permafrost controls subsurface gas transfer is difficult in polar deserts, where direct observations of thaw state and permeability are logistically limited. Here we test whether paired soil-gas measurements of radon (^{222}Rn) and thoron (^{220}Rn) can be used to distinguish shallow active-layer production from deeper advective gas transport in Taylor Valley, Antarctica. We carried out a systematic grid survey at 149 sites during two austral summers (2019/20 and 2023) and combined field measurements with laboratory determinations of radionuclide content and radon/thoron exhalation from active-layer sediments. The two isotopes behaved differently. ^{220}Rn, which decays very rapidly, was consistent with a dominantly shallow source, although field values were systematically lowered by sampling dilution. By contrast, ^{222}Rn did not scale with shallow production alone, and the highest field concentrations exceeded the locally constrained equilibrium range expected from the active layer. This indicates an additional transport component, most plausibly linked to upward gas migration from below the active layer. The strongest ^{222}Rn anomalies were more widespread in 2019/20 compared with the colder 2023 campaign, suggesting that short-term meteorological conditions can modulate subsurface connectivity and gas transport efficiency. These results show that radon isotopes provide a practical framework for identifying shallow versus deeper gas pathways and for monitoring climate-sensitive changes in Antarctic permafrost systems.

1. Introduction

Radon is a naturally occurring radioactive gas that can be used as an environmental tracer, offering insights into geological and environmental processes. Among the 39 known radon isotopes (from ^{219}Rn to ^{231}Rn), only two, ^{222}Rn and ^{220}Rn, occur in significant amounts and are commonly used in environmental sciences (Nazaroff and Nero Jr, 1987). Radon (^{222}Rn), a product of the ^{238}U decay chain, is the most abundant isotope in enclosed environments due to its relatively long half-life (3.82 days). Thoron (^{220}Rn), a nuclide of the ^{232}Th series, decays rapidly

* Corresponding author. National Research Council, Infrastructures Research Office, CNR-UIR, Roma, Italy.
E-mail address: livio.ruggiero@cnr.it (L. Ruggiero).

https://doi.org/10.1016/j.envres.2026.124523
Received 30 January 2026; Received in revised form 20 March 2026; Accepted 14 April 2026
Available online 16 April 2026
0013-9351/© 2026 The Authors. Published by Elsevier Inc. This is an open access article under the CC BY license (http://creativecommons.org/licenses/by/4.0/).

(half-life of 55.6 s) but can often reach higher concentrations in soil gas, as thorium is generally more abundant in the Earth's crust than uranium. Because of their differing half-lives, each isotope migrates over different distances. Due to its very short half-life, ^{220}Rn mainly reflects near-surface production and very local transport conditions, and is therefore strongly influenced by soil properties such as porosity, permeability, moisture, soil texture and pore-scale structure. This limits the applications of ^{220}Rn primarily to near-surface investigations (Garland et al., 1993; Tositti et al., 2002; Puzzilli et al., 2024). In contrast, ^{222}Rn can accumulate in pore spaces and requires a carrier gas for long-distance transport (Etiope and Lombardi, 1995; Sciarra et al., 2018; Benà et al., 2022). ^{222}Rn transport over wider distances occurs mainly via advection, supported by the gas flux like CO_2 or CH_4 (Kristiansson and Malmqvist, 1982; Etiope and Martinelli, 2002; Yuce et al., 2010, 2017; Sciarra et al., 2018). Since ^{220}Rn and ^{222}Rn respond to processes at different spatial scales (Huxol et al., 2013), ^{222}Rn can reveal deeper subsurface gas movements and geological processes, including fault dynamics, and can be used as an earthquake precursor, and in volcanic monitoring (Etiope and Martinelli, 2002; Vaupotič et al., 2010). These properties make it a valuable tool for detecting active faults in tectonically active areas (King et al., 1996; Ciotoli et al., 1999, 2016; Toutain and Baubron, 1999; Etiope and Martinelli, 2002; Walia et al., 2005; Yang et al., 2005; Yuce et al., 2010, 2017). Lastly, if ^{222}Rn accumulates in closed or confined spaces, it is very harmful to human health and is the second leading cause of lung cancer after cigarette smoke (Samet, 1989; Sethi et al., 2012; Giustini et al., 2022).

Given its sensitivity to changes in subsurface permeability, radon also provides a powerful means to investigate environments where ground thermal state and freeze–thaw cycles strongly regulate gas mobility. Permafrost, which is soil or sediment permanently frozen for at least two consecutive years, covers significant portions of Earth's surface: 24% of the Northern Hemisphere, and around 0.2% of the Southern Hemisphere (0.4% in Antarctica; Bockheim et al., 2007). Permafrost profoundly affects radon dynamics, acting as an effective barrier that significantly reduces radon gas migration (Sellmann and Delaney, 1990; Glover and Blouin, 2022). Field and laboratory studies have confirmed that soil radon concentrations above permafrost areas can be substantially lower than in adjacent unfrozen ground with surface radiation exposure above frozen ground about one-tenth of background levels (Sellmann and Delaney, 1990; Klimshin et al., 2010; Zhang et al., 2024). Freezing conditions do not prevent the decay of uranium into radon, but the permafrost layer acts as a “plug” preventing the radon generated in the underlying rock substrate from reaching the surface. This same barrier also causes a tenfold increase in radon activity beneath it, creating an “accumulated reservoir” of radon. This reservoir represents a potential health threat when the permafrost begins to thaw. With ongoing climate change and associated permafrost degradation, there is growing concern about increasing radon exposure in polar and high-altitude regions, particularly as thawing permafrost releases accumulated radon (Puchkov et al., 2021; Zhang et al., 2024). Modelling studies predict significant rises in radon fluxes as permafrost integrity deteriorates, posing potential health risks, especially in poorly ventilated buildings in Arctic communities (Glover and Blouin, 2022; Zhang et al., 2024).

Recent research highlights radon as a promising tracer for assessing permafrost integrity, as variations in soil radon concentrations can effectively reflect thaw-induced changes in soil permeability (Glover and Blouin, 2022; Zhang et al., 2024). Although permafrost is less extensive in the Southern Hemisphere, regions such as Antarctica represent unique environments for investigating radon dynamics. The Antarctic Peninsula, experiencing rapid warming, has exhibited notable seasonal variations in radon flux correlated with thawing permafrost (Tositti et al., 2002). Since Antarctica is largely covered by ice, few areas characterized by continuous permafrost can be monitored; the McMurdo Dry Valleys are one of the ideal localities where the impact of global warming can be investigated on ice-free regions (Carshalton et al., 2022).

Despite the growing interest in radon as a tracer of permafrost integrity, it remains difficult to separate radon produced within the shallow active layer from radon supplied through deeper gas pathways. This distinction is critical, because shallow production reflects local sediment properties, whereas excess ^{222}Rn may indicate enhanced subsurface connectivity beneath the permafrost. Taylor Valley represents an exceptional natural laboratory to test these mechanisms because it combines continuous permafrost, strong interannual meteorological variability, and accessible ice-free terrain. In polar deserts, direct observations of thaw state and subsurface connectivity are logistically challenging, creating the need for field-ready tracers that integrate transport efficiency at relevant spatial scales. Here we combine repeated field measurements of ^{222}Rn and ^{220}Rn with laboratory constraints on radionuclide content and exhalation from active-layer sediments to determine whether anomalous ^{222}Rn can be explained by shallow production alone or requires an additional deeper transport component. More broadly, this study develops a transferable and field-practical framework for detecting climate-sensitive changes in subsurface connectivity in Antarctic permafrost landscapes.

2. Methodology

2.1. Study area and grid selection

The McMurdo Dry Valleys (MDV) encompass a diverse landscape that includes ice-covered lakes, ponds, ephemeral streams, valley glaciers, and sediments of glacial, fluvial, lacustrine, and aeolian origin (Fig. 1). The mean annual air temperature is approximately −17 °C, while annual precipitation, measured as snow water equivalent, ranges between 3 and 50 mm (Fountain et al., 2010), classifying the MDV as a cold polar desert (Monaghan et al., 2005). Permafrost, which underlies 90–100% of the MDV, is primarily ice-cemented, varying from ice-saturated to weakly cemented. In Taylor Valley, ice-cemented permafrost is the dominant frozen-ground type, particularly in the eastern half of the valley and adjacent to alpine glaciers, whereas dry-frozen permafrost is more typical of valley walls (in the upper ~1 m) and more inland sectors (Bockheim et al., 2007). At the regional scale, buried ground ice and ice-cored deposits are known from several sectors of the MDV (Hall and Denton, 2000; Bockheim et al., 2007; Swanger et al., 2010), but their detailed distribution is not mapped within the present survey grid and is therefore not used here as a direct explanatory variable. Taylor Valley (77°37′ S, 163°15′ E) is the southernmost of the three principal Dry Valleys in the Transantarctic Mountains, stretching ~29 km WSW-ENE from Taylor Glacier to McMurdo Sound (Fig. 1).

The surveyed sector lies in the lower Taylor Valley, extending ~6 km eastward from Lake Fryxell and bordering the southern edge of the Commonwealth Glacier (Fig. 2). Fig. 1 provides the regional location of this sector within Taylor Valley, whereas Fig. 2 shows the local sampling grid and measurement sites. Measurements were performed at the contact between the active layer and the permafrost table; therefore, the sampling depth at each site corresponds to the local active-layer thickness at the time of the survey, and ranged from 15 to 60 cm across the grid. This area features hummocky moraines, lacustrine deposits, and outwash fans where ephemeral streams and water tracks are active during the summer months. These unconsolidated surficial deposits constitute the shallow sedimentary framework directly relevant to soil-gas production and transport through the active layer. In addition to the shallow sedimentary framework, the deeper subsurface beneath lower Taylor Valley is known to include thick permafrost overlying saline groundwater/brine systems. Early borehole and geophysical investigations, including DVDP-11 and resistivity soundings, already suggested this hydrogeologic configuration (McGinnis and Jensen, 1971; McGinnis et al., 1981), and more recent airborne electromagnetic and electric resistivity studies have confirmed the presence of low-resistivity brines at multiple levels beneath the Fryxell basin and the

Fig. 1. Location of the study area (red ellipse) in lower Taylor Valley, McMurdo Dry Valleys (Victoria Land, East Antarctica). Geographic coordinates (WGS84) are shown on the map frame. The positions of the meteorological stations used in this study (EXEM and FRLM) are also indicated. Basemap credit: Google Earth (accessed March 2026). (For interpretation of the references to color in this figure legend, the reader is referred to the Web version of this article.)

eastern sector of Taylor Valley (Mikucki et al., 2015; Foley et al., 2019; Romano et al., 2024). These deeper conditions represent a relevant background to interpret possible advective gas pathways, although their detailed geometry is not resolved at the scale of the present sampling grid. Our measurements were conducted following a regular 250 × 250 m grid covering a surface of 21 km^2 and comprising 149 stations. In the eastern and southern sectors of the study area, sample spacing increased to approximately 500 m (Fig. 2). The sampling strategy was designed to balance logistical constraints with the goal of obtaining representative data from the study area (see Ruggiero et al., 2023 for more details about the grid selection).

2.2. Soil gas survey

^{222}Rn and ^{220}Rn activities were measured in soil gas at the interface between the active layer and the permafrost table, at depths of 15-60 cm, by inserting a hollow stainless-steel probe vertically into the soil (Fig. 3A and B). The probe tip had small lateral holes to allow gas to enter freely from the surrounding soil. The probe was connected via vinyl tubing to a portable RAD7 (Durridge Company Inc.), which simultaneously measures ^{222}Rn and ^{220}Rn concentrations. Durridge RAD7 uses a silicon semiconductor detector and has a calibration range of 4 to 400,000 Bq/m^3 with a sensitivity of 0.0067 cpm/(Bq/m^3). The manufacturer-reported ±5% value refers to nominal instrument accuracy under controlled conditions; in practice, field uncertainty depends on counting statistics, activity level, humidity, and integration time. The detector performs alpha spectrometry of short-lived radon progeny. In particular, ^{222}Rn is quantified through the alpha-emitting daughters ^{218}Po and ^{214}Po, whereas ^{220}Rn is detected through its short-lived daughter ^{216}Po. The instrument has an electrostatic chamber with a volume capacity of 0.7 L and gas is introduced by means of a 1 L/min membrane pump. Pumping may perturb the near-probe gas field and may induce variable mixing with atmospheric air, depending on soil texture, permeability, and sealing around the probe. The magnitude of this perturbation may also vary with sampling depth, especially at shallowest sites. In our case, the dominant concern is not artificial enrichment but rather dilution and transfer losses, particularly for ^{220}Rn. Because thoron has a 55.6 s half-life, its measured activity is especially sensitive to transit time, tubing length, humidity, and the overall sample-transfer configuration. For this reason, the tubing between probe and detector was kept as short as practically possible and ^{220}Rn data are interpreted conservatively as a shallow tracer and qualitative indicator of dilution. A single measurement takes an average of 20 min, with four consecutive 5-min partial readings. Final concentrations of both ^{222}Rn and ^{220}Rn were calculated as the average of the last two readings, following standard RAD7 soil-gas acquisition practice, in which the initial cycles are discarded to allow flushing of the tubing and chamber and equilibration of the sampled gas volume. A desiccant trap (drierite; $CaSO_4$) and an inlet dust filter protect the detector from high relative humidity (RH >10%) and particles. Moreover, for radon activity it has been possible to define a geochemical threshold, based on the ^{222}Rn activity at equilibrium with parent radionuclides (^{226}Ra) in the surveyed soil, from the formula (Åkerblom, 1993):

$$C_{Rn} = C_{Ra}\varepsilon\rho n^{-1} \quad (1)$$

where C_{Rn} and C_{Ra} are radon and radium concentrations, respectively, in soil gas (Bq/m^3) and in soil (Bq/kg), ε is the emanation power coefficient (dimensionless), ρ is soil density (kg/m^3), and n is the effective porosity coefficient (dimensionless).

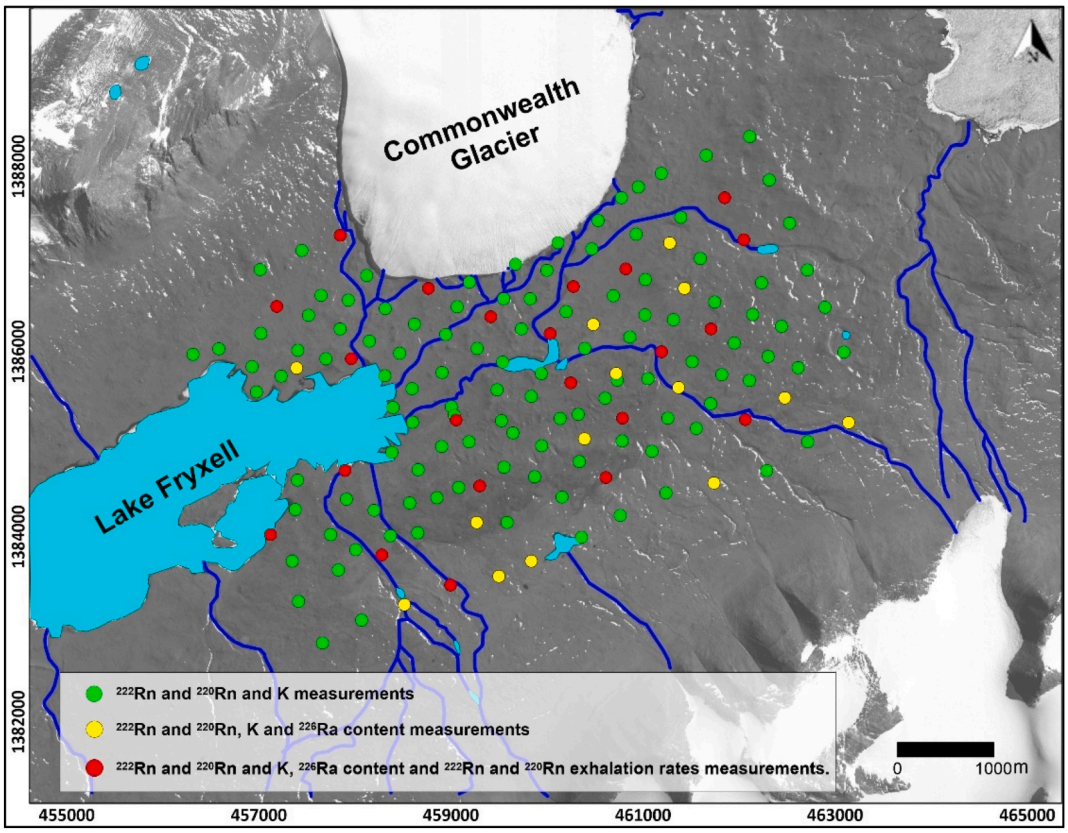

Fig. 2. Map of sampling locations and measurement types (coordinates in WGS84/UTM Zone 58S, metres). In-situ measurement sites for ^{222}Rn, ^{220}Rn and permeability (K) are shown in green; sites where soil samples for radionuclide analysis were collected are shown in yellow; and sites where samples for exhalation rate measurements were collected are shown in red. The area was surveyed during two austral summer campaigns, in 2019/20 and 2023. (For interpretation of the references to color in this figure legend, the reader is referred to the Web version of this article.)

2.3. Soil permeability

Soil intrinsic permeability (k, Fig. 3C) was measured using the PRM3-2 permeameter (Castelluccio et al., 2015; Lucchetti et al., 2019). This device, equipped with a battery, a membrane pump and a vacuum gauge with digital display, was connected to the same probe used for the soil gas survey. Permeability measurements were therefore performed at the same depth and in the same thawed sediments sampled for ^{222}Rn and ^{220}Rn, i.e. at the contact between the active layer and the permafrost table. Consequently, the measured k values refer to the shallow unfrozen sediment immediately overlying the frozen substrate, rather than to the permafrost matrix itself. Since PRM3-2 was calibrated using hollow Radon v.o.s. probes (https://www.radon-vos.cz/) equipped with disposable tips which could not be left in Antarctica, a specific calibration of the permeameter was carried out with the probes specifically employed there (Stefanelli, 2021). These measures were intended to characterize the permeability of the final shallow pathway through which soil gas must pass before reaching the surface, and therefore to provide an independent descriptor of local near-surface transport conditions.

2.4. Exhalation rates of ^{222}Rn and ^{220}Rn

Approximately 400 g of soil was collected at the contact between the active layer and the permafrost table, i.e. at the same stratigraphic interface targeted by the *in-situ* soil-gas measurements, in order to constrain the shallow source term through laboratory analyses of radionuclide content and radon/thoron exhalation. The samples were dried at 100 °C for 24 h and transferred for 15 min to a sealed Polyvinyl Chloride (PVC) box to cool without absorbing moisture from the air. This was done to prevent moisture absorption in the pores thus affecting radon and thoron exhalation (Lucchetti et al., 2019). Samples were then introduced into a 5.1 L stainless steel accumulation chamber (Tuccimei et al., 2009), which had been pre-purged to reduce the humidity in the test circuit below 10%. Under these conditions, the experimental set-up is not affected by radon leakage or back-diffusion phenomena (Tuccimei et al., 2009). It comprised a radon monitor (RAD7, Durridge Company, Inc., Billerica, MA, USA) connected via vinyl tubing to the accumulation chamber, which was placed in a thermo-refrigerating bath filled with water at 30 °C. The bath ensured constant exhalation temperature for all samples, with radon exhalation being directly proportional to temperature (Tuccimei et al., 2006; Mollo et al., 2021, Fig. 3D, E, F, G, H). These laboratory conditions were intentionally standardized to allow inter-sample comparison of the shallow source term, rather than to reproduce the full range of *in-situ* thermal and moisture conditions encountered at the permafrost table. ^{222}Rn and ^{220}Rn activity concentration in the circuit was monitored hourly for 18 h and ^{222}Rn (E^{222}) and ^{220}Rn (E^{220}) exhalation rates (Bq/m^2 h^1) were calculated using equations (2) and (3) (Tuccimei et al., 2009):

$$E^{222} = (m + \lambda^{222} + C_0) \cdot V / S \quad (2)$$

$$E^{220} = (\lambda^{220} \cdot V_0) \cdot (C_m / (e^{-\lambda 220 \cdot (V1/Q)}) \quad (3)$$

where m is the slope of the ^{222}Rn growth curve (Bq/m^3 h^1), λ^{222} and λ^{220} are ^{222}Rn and ^{220}Rn decay constant (h^{-1}), C_0 and C_m are respectively the initial ^{222}Rn and the average ^{220}Rn activity concentrations (Bq/m^3), V, V_0 and V_1 are respectively the free total volume of the analytical system, the volume of the accumulation chamber and the volume of the tubing connecting the accumulation chamber to the RAD7 (m^{-3}), S is the surface of the accumulation chamber (m^2) and Q is the flow rate in the

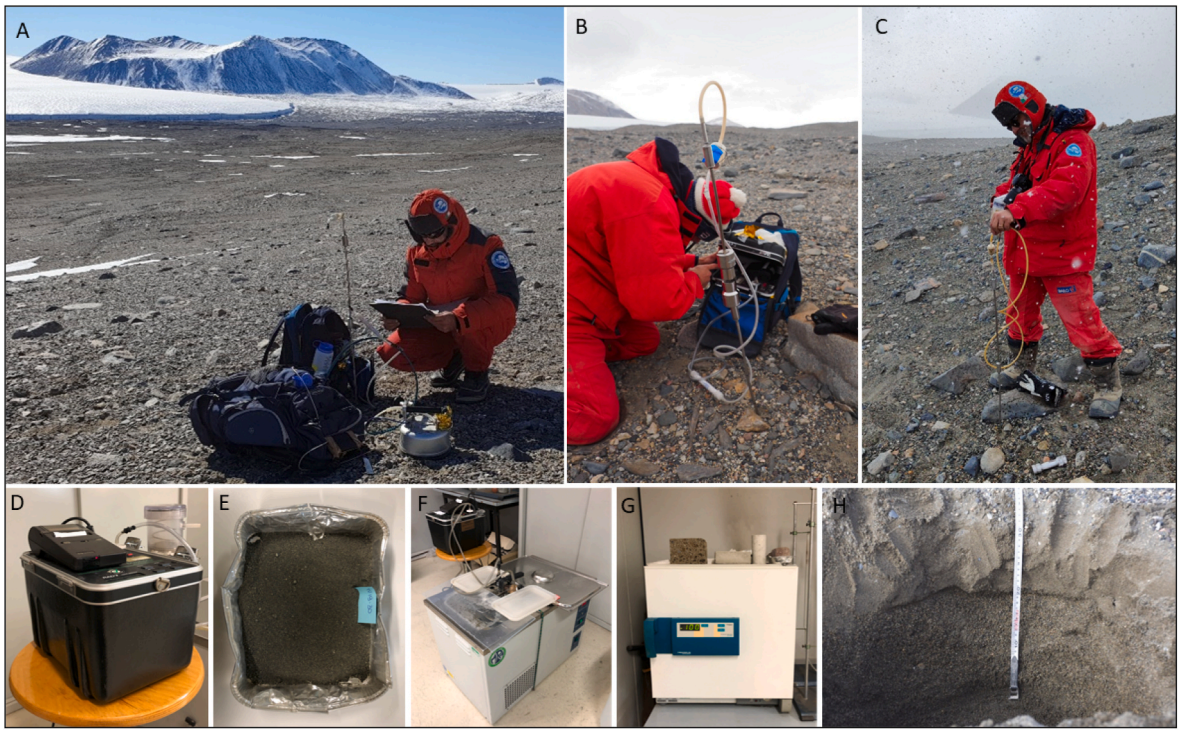

Fig. 3. Overview of the experimental methodology and field measurements: A) Measurement of ^{222}Rn and ^{220}Rn in 2019/20. B) Measurement of ^{222}Rn and ^{220}Rn and C) measurement of intrinsic soil permeability in 2023. D) Durridge RAD7 used for radon exhalation measurements. E) Crushed and dried soil sample ready for analysis. F) Accumulation chamber placed in a thermo-refrigerating bath filled with water at 30 °C. G) Oven used for drying the samples. H) Soil profile from which a sample was collected.

system (m^3/h^1). Because of its 55.6 s half-life, ^{220}Rn exhalation is more sensitive than ^{222}Rn to pore-scale transfer conditions, sample microstructure, and the presence of moisture or ice. We therefore acknowledge that fine-scale differences between field and laboratory conditions may affect the absolute comparability of ^{220}Rn exhalation rates. However, the laboratory setup and Eq. (3) explicitly account for decay and transfer effects through the analytical circuit (including the tubing volume and system flow rate), so that E_{220} still provides a standardized and internally consistent estimate of the shallow thoron source term. For this reason, ^{220}Rn exhalation data are used here as a constraint on shallow production, while their interpretation is kept conservative when directly compared with field measurements under natural frozen-ground conditions.

Uncertainties in exhalation rates depend mainly on the error associated with the regression coefficient of the ^{222}Rn growth curve and the standard error of the mean of the ^{220}Rn data. Errors were calculated with OriginPro 9 (OriginLab Corporation, Northampton, MA, UNITED STATES). These laboratory measurements were used to constrain the shallow active-layer source term across the study area and to quantify the expected range of production-derived ^{222}Rn and ^{220}Rn concentrations for comparison with the in-situ soil-gas dataset.

2.5. Radionuclide content

To constrain the lithogenic source term of soil-gas radon, we characterized the activity of the relevant decay-chain radionuclides in the sampled sediments by gamma spectrometry. In particular, ^{222}Rn is generated from ^{226}Ra, whereas ^{220}Rn is generated from ^{224}Ra within the ^{232} Th decay series. Accordingly, the gamma-spectrometric dataset was used to quantify bulk radionuclide activity in the sediments, with particular emphasis on ^{226}Ra for the production-based ^{222}Rn equilibrium calculations and on ^{228}Ac as an indirect proxy for the ^{232}Th series relevant to ^{220}Rn production. To this end, 36 soil samples were collected across the campaign in 2019/20 at the same stations where soil-gas were measured.

Prior to γ-spectrometry analysis, soil samples were crushed, sieved at 2 mm, and placed into polystyrene jars. Samples were analysed using a p-type extended range coaxial Hyper Pure Germanium (HPGe) crystal detector (PROFILE, Ortec-Ametek Inc., measuring range: 20-2000 keV). The detector has a relative efficiency of 20% and a resolution (FWHM) of 1.9 keV at 1332.5 keV. The system was calibrated for energy and efficiency using a multi-radionuclide liquid source (QCYA48, Eckert & Ziegler Nuclitec GmbH) in a jar geometry (diameter = 56 mm and thickness = 10 mm). Spectra were acquired for 80,000 s to optimize peak analysis and were subsequently processed with the Gamma Vision-32 software (version 6.07, Ortec-Ametek).

Uncertainty (here defined as one standard deviation) on peak areas was calculated by propagating the combined error of the previously determined efficiency fit and counting statistics. The minimum detectable activity was determined using the Traditional ORTEC method (ORTEC, 2003) with a peak cut-off limit of 40%. Certified reference materials (DH-1a and UTS-3, CANMET) were used to verify measurement quality.

We note that bulk radionuclide activity in the sediment is not identical to the fraction of radium effectively available at grain surfaces for radon release, particularly for the very short-lived ^{220}Rn. For this reason, gamma spectrometry is used here to constrain the overall lithogenic source domain in the sediment, whereas the exhalation experiments provide the process-relevant link to actual radon and thoron release. In addition, the use of parent-chain activities as a proxy for radon precursors assumes near-secular equilibrium within the measured decay chains. In the present hyper-arid Antarctic setting, where the sampled sediments are old and modern hydrological reworking is limited, this is treated as a reasonable first-order approximation, while remaining an explicit limitation of the approach. Accordingly, the gamma-spectrometric dataset is interpreted more cautiously for ^{220}Rn than for ^{222}Rn, and thoron-related inferences are discussed jointly with the laboratory exhalation results. For ^{222}Rn, the gamma-derived radionuclide

dataset and the laboratory exhalation results were also used jointly to derive a site-specific production-based equilibrium reference for comparison with field concentrations. Details on the methods and checks used for the determination of ^{238}U and ^{232}Th radionuclides are available elsewhere (Tositti et al., 2017, 2020; Cinelli et al., 2015). Briefly, ^{226}Ra was determined from the 186 keV photopeak after correction for ^{235}U interference, assuming secular equilibrium between ^{226}Ra and ^{238}U and a natural ^{235}U/^{238}U isotopic ratio. ^{238}U and ^{232}Th were then inferred from the gamma emissions of their daughter radionuclides, using ^{226}Ra for the ^{238}U series and ^{228}Ac for the ^{232}Th series (Gilmore and Joss, 2024).

2.6. Statistical and geostatistical analysis

2.6.1. Exploratory statistics

Exploratory Data Analysis (EDA), utilizing both numerical and graphical methods, was employed to analyze soil gas data, characterize soil-gas data and support subsequent anomaly and spatial modelling. For each variable and campaign (^{222}Rn, ^{220}Rn, sampling depth, and permeability where available), we calculated standard descriptive statistics (minimum, maximum, mean, median, standard deviation, coefficient of variation, and selected quantiles) and distribution-shape metrics (skewness and kurtosis) to assess central tendency, dispersion, and tail behaviour. Graphical inspection included histograms, density plots, boxplots and quantile–quantile/normal probability plots to evaluate departure from normality and the presence of multiple populations.

In consideration of the characteristically right-skewed nature of soil-gas concentrations, radon and thoron were analysed in both their original units and following natural-log transformation (ln^{222}Rn; ln^{220}Rn). The log transformation stabilised variance and reduced the influence of extreme values, yielding distributions closer to Gaussian and better aligned with the assumptions underlying spatial autocorrelation statistics and geostatistical interpolation. Log-transformed variables were primarily used for geostatistical modelling, as well as for defining statistical populations and thresholds. We conducted inter-annual comparisons by examining the differences between 2019 and 2023 at matched locations and by analysing derived variables (e.g., ΔRn, ΔTn) where appropriate. Throughout EDA, we verified data integrity (missing values, duplicates, coordinate consistency, and plausible ranges) and treated anomalous/extreme values as candidate signals rather than automatically removing them.

Normal probability plots (NPPs) were interpreted using the Sinclair method (Sinclair, 1991) to identify distinct statistical populations and derive anomaly thresholds for each gas species. Linear segments on the NPP were interpreted as separate lognormal populations, and breakpoints between segments were used to define background and anomalous classes in a reproducible, distribution-based manner.

2.6.2. Spatial statistics

Since correlation analyses and anomaly detection can be affected by how observations are related in space, spatial autocorrelation was quantified using global and local spatial statistics to evaluate whether the sampling design exhibits spatial dependence (and thus violates the independence assumption underlying correlation and anomaly analyses). All computations were performed in projected coordinates (WGS84/UTM zone 58S; distances in meters) using a fixed-distance spatial weights matrix. The neighbourhood distance was selected using Incremental Spatial Autocorrelation (ISA) by identifying the distance at which the Global Moran's *I* *z*-score reached its maximum. Based on the outcomes of the Incremental Spatial Autocorrelation (ISA) analysis and to ensure comparability across variables and surveys, a fixed-distance band of 2.0 km was adopted for all analysis. Global Moran's *I* was used to quantify global spatial autocorrelation, and to provide an overall measure of spatial dependence (i.e., positive clustering versus spatial randomness). Furthermore, Getis–Ord General *G* was used to determine whether the spatial pattern was characterised by clusters of high or low concentrations. Local spatial clustering was mapped using Getis–Ord *Gi** hot-spot analysis to identify statistically significant hot spots (areas with high values surrounded by high values) and cold spots (areas with low values surrounded by low values).

Statistical significance for the global tests (Moran's *I* and Getis–Ord General *G*) was assessed using 999 permutations, by comparing the observed statistics with a randomisation distribution under the null hypothesis of spatial randomness. For the *Gi** local statistic, *p*-values were adjusted for multiple comparisons using a False Discovery Rate (FDR) correction (Benjamini–Hochberg procedure), and only locations remaining significant after FDR correction were mapped and discussed. This approach reduces the number of false positives expected when testing many locations simultaneously, while preserving sensitivity to spatially coherent clusters. Spatial statistics were applied consistently to both raw and log-transformed variables where relevant (particularly for Rn/Tn). This allowed us to: a) diagnose spatial dependence at the scale of the sampling design; b) avoid over-interpreting purely local extremes; and c) provide an independent line of evidence for spatial clustering that complements the distribution-based NPP classification.

2.6.3. Depth-only baseline and correction for sampling depth

Gas concentrations in the soil may show a systematic dependence on sampling depth. Shallower samples are more influenced by exchange with the atmosphere and by thermo-hygrometric conditions. The literature documents that radon concentration in soil gases tends to increase with depth, with gradients linked to diffusion/transport and physical soil conditions (Nazaroff, 1992; Shweikani et al., 1995; Smetanová et al., 2010; Yang et al., 2019; Mao et al., 2023; Leshukov et al., 2024).

To separate this systematic effect from horizontal spatial variability, we constructed a depth-only baseline based on simple linear regression:

$$\ln(C_i) = \alpha + \beta^{*}Depth_i + \varepsilon_i \quad (4)$$

where $\ln(C_i)$ is the natural logarithm of the concentration (Rn or Tn) at point *i*, $Depth_i$ is the sampling depth and ε_i is the residual. For each year (2019/20 and 2023), the following were calculated: (i) the area of the trend with depth through the predicted values ln(C), and (ii) the depth-corrected residuals $\varepsilon_i = \ln(\,) - \widehat{\ln(\,)}$. The depth-only baseline was evaluated with cross-validation (the same scheme adopted for geostatistical models), reporting ME (bias), MAE, and RMSE calculated on the prediction residuals. This baseline has a dual purpose: (1) to provide a "minimum" and physically interpretable reference for predictive power linked exclusively to depth; (2) to prevent "forced" variography or kriging from capturing a vertical trend as if it were horizontal spatial autocorrelation.

To move from point correction for depth to the construction of continuous maps, we adopted a geostatistical regression-kriging approach (EBKRP), which incorporates depth as an explanatory variable and interpolates the residuals using Bayesian kriging.

2.6.4. Empirical Bayesian Kriging Regression Prediction (EBKRP)

Empirical Bayesian Kriging (EBK) was used to produce maps and, when an explanatory predictor was available, its extension Empirical Bayesian Kriging Regression Prediction (EBKRP) was also used. EBK is a geostatistical method implemented in ArcGIS Geostatistical Analyst that estimates the interpolated surface by modeling spatial autocorrelation using "local" variograms and incorporating the uncertainty of the variogram parameters with an empirical-Bayesian approach (Pilz and Spöck, 2008; Krivoruchko, 2012; Krivoruchko and Gribov, 2019; Samsonova et al., 2017; De Risi et al., 2021). Rather than assuming a single known 'true' variogram, EBK generates and combines multiple variogram and prediction estimates, which often results in robustness in the presence of relatively small datasets and/or moderate local non-stationarity.

EBKRP combines a deterministic component (regression on covariates) and a stochastic component (kriging of residuals) (Cressie, 1993;

Hengl et al., 2007; Giustini et al., 2019; Coletti et al., 2022). Operationally, EBKRP:

- estimates a relationship between the response variable and one or more predictors (e.g., depth);
- calculates the regression residuals;
- interpolates the residuals with EBK;
- reconstructs the final prediction as the sum of the trend + kriged residual.

In the present study, EBKRP was applied using sampling depth (Prof_2019/20 and Prof_2023) as a predictor, with the aim of (i) reducing the vertical systematic component, (ii) making the residual spatial structure more interpretable, and (iii) quantitatively verifying whether the inclusion of depth improved performance compared to "pure" EBK and the depth-only baseline. EBKRP supports the use of explanatory rasters and includes procedures to manage collinearity between covariates (e.g., using principal components when necessary).

The final choice of mapping model was guided by cross-validation results and standard diagnostic indicators provided by geostatistical tools (ME, RMSE, MAE; and standardized statistics/predictive interval coverage), comparing EBK vs EBKRP and, in parallel, verifying that EBKRP also improved the depth-only baseline.

Because EBKRP requires explanatory variables as continuous surfaces, a depth raster was generated separately for each campaign (2019/20 and 2023) by interpolating point-measured sampling depths using radial basis functions (RBF) and masking the resulting surface to the study-area polygon. EBKRP prediction outputs were then used to derive contour maps of predicted ln-concentrations. Model performance was evaluated using leave-one-out cross-validation; summary diagnostics (ME, RMSE, mean standardized error, RMS standardized error, and average standard error) are reported in Table S1.

2.7. Meteorological data and barometric pressure

Daily meteorological conditions during the two campaigns were characterized using records from two McMurdo Dry Valleys LTER automatic weather stations located in Taylor Valley: Explorers Cove (EXEM; 77.588733° S, 163.417523° E, Dugan et al., 2025a) and Lake Fryxell (FRLM; 77.611300° S, 163.170100° E, Dugan et al., 2025b). Their locations relative to the surveyed sector are shown in Fig. 1. Available data include air temperature at 3 m, soil temperature at 10 cm, wind speed and relative humidity. For each sampling day, air temperature, soil temperature, and wind speed were calculated as the arithmetic mean of the corresponding records from the two stations, in order to represent the overall meteorological conditions affecting the surveyed sector. To capture short-term atmospheric forcing on soil–gas transport, barometric pressure (hPa) was recorded at each flux measurement using the digital barometer integrated in the WEST Systems portable fluxmeter/accumulation chamber. The chamber hosts a pressure–temperature–relative humidity sensor mounted on the chamber ceiling; pressure is measured by a digital barometer (Freescale MPL3115A2; operating range 500–1100 mbar; stated accuracy ±0.5 mbar, i.e., hPa). To avoid chamber pressurization during measurements, the accumulation chamber includes a pressure-compensation vent that maintains pressure equilibrium between the chamber headspace and the outside air; therefore, the recorded pressure is representative of ambient barometric pressure during each acquisition.

3. Results

3.1. Soil gas survey and permeability

The soil-gas survey conducted at 149 sampling sites revealed clear differences in the behaviour of ^{222}Rn and ^{220}Rn between the two campaigns. In both years, ^{222}Rn displayed broad spatial variability, but the 2019/20 dataset showed a greater frequency of high-concentration values and a more pronounced upper tail compared with the 2023 survey. By contrast, ^{220}Rn was consistently characterized by higher absolute activities than ^{222}Rn in both campaigns, with marked variability and a broader range in 2019/20 than in 2023. Sampling depth, corresponding to the active-layer thickness, remained within a relatively narrow interval in both years, while permeability measured in 2023 indicated comparatively homogeneous shallow transport conditions across the study area. Matched-point interannual comparisons (Fig. S1) indicate that year-to-year correspondence is more pronounced for ^{222}Rn than for ^{220}Rn, the latter showing a more scattered site-by-site response between campaigns. Interestingly, although high-activity values are less frequent in 2023, the maximum concentrations observed in the two campaigns remain broadly comparable in magnitude, suggesting that the main difference between surveys lies more in the frequency and spatial extent of anomalies than in their absolute upper bound.

3.1.1. Exploratory statistics

Descriptive statistics summarizing all measured parameters are detailed in Table 1. The 2023 distributions of ^{222}Rn and ^{220}Rn activities, together with soil permeability and permafrost depth data from both surveys, were well described by log-normal distributions, as demonstrated by comparable median and geometric mean (GM) values. Moreover, the Kolmogorov–Smirnov test confirmed these log-normal distributions ($p > 0.01$), notwithstanding positive skewness evident in the datasets. Activity concentrations for ^{222}Rn in the 2023 campaign ranged from 110 to 2008 Bq/m^3, while the 2019/20 campaign showed a narrower range (15 to 1830 Bq/m^3) with slightly higher average values. For ^{220}Rn, 2023 concentrations ranged between 2769 and 20,944 Bq/m^3, and the earlier 2019/20 campaign exhibited greater variability (145 to 27,589 Bq/m^3) and higher average values.

Permafrost depth measurements indicated consistency across both survey periods, suggesting relatively stable soil conditions. Permeability data for the shallow thawed material at the active-layer base, collected only in 2023 at the same sampling points as the previous survey, also revealed homogeneous conditions throughout the study area.

Histograms of radon isotope distributions (Fig. S2) provide clear visual representations of the differences in variability and concentration patterns between the two isotopes and across the two temporal periods. Specifically, the distribution of ^{222}Rn activity in the 2019/20 campaign showed substantial variability with a pronounced frequency of higher concentrations, primarily in the 400–600 Bq/m^3 range but extending considerably towards higher values up to 2000 Bq/m^3. In contrast, the 2023 dataset was more tightly clustered, predominantly around the 400–600 Bq/m^3 range, demonstrating fewer occurrences at elevated concentrations. The distributions of ^{220}Rn were consistently right-skewed in both survey periods, yet the 2023 data notably displayed fewer instances of extremely high concentrations compared to 2019/20.

The frequency histograms for permafrost depth in 2019/20 and 2023 reveal that both periods have a relatively similar ice table depth distribution with a mode centered on 30 cm and a few measurements up to 50 cm (2019/20) and 60 cm (2023). For permeability, the histogram shows a left-skewed distribution, with a peak around 1.6×10^{-7} cm^2 suggesting that most of the sampled ground materials have low permeability.

The NPP for both the ^{222}Rn and ^{220}Rn data from 2019/20 and 2023 are insightful tools for examining the distribution and potential anomalies in radon isotopes concentrations over the years. In both plots, the observed radon concentrations are plotted against the expected normal values to highlight potential outliers or abnormal trends. Fig. 4 shows the background values from the anomalous ones for ^{222}Rn and ^{220}Rn: 580 Bq/m^3 for ^{222}Rn in 2023, 700 Bq/m^3 for ^{222}Rn in 2019/20, and 12,500 Bq/m^3 for ^{220}Rn in both 2023 and 2019/20. ^{222}Rn levels were substantially higher in 2019/20 compared to 2023. The 2023 dataset, although still displaying some deviations at higher concentrations, shows a smaller anomaly, indicating relatively lower radon levels and

Table 1
Descriptive statistics of soil ^{222}Rn and ^{220}Rn concentrations in 2019/20 and 2023, sampling depth in 2019/20 and 2023 and permeability in 2023; N: number of samples; Mean: Arithmetic mean; GM: Geometric mean; Min: Minimum value; Max: Maximum value; LQ: Lower quartile; UP: Upper quartile; P10%: 10th percentile; P90%: 90th percentile; Std.Dev: Standard deviation; SK: Skewness.

Variable	N	Mean	GM	Median	Min	Max	LQ	UP	P10%	P90%	Std.Dev.	SK
^{222}Rn 2023 Bq/m^3	149	487	433	422	110	2008	319	620	238	796	261	2.08
^{222}Rn 2019/20 Bq/m^3	149	571	467	519	15	1837	321	749	187	998	336	1.07
^{220}Rn 2023 Bq/m^3	149	8992	8458	8365	2769	20944	6894	10628	5297	13011	3225	1.07
^{220}Rn 2019/20 Bq/m^3	149	10275	9144	9634	145	27589	7427	11841	5790	16681	4436	0.97
Sampling depth 2023 cm	149	31	30	30	20	60	27	35	25	40	6	0.92
Sampling depth 2019/20 cm	149	30	29	30	15	50	25	33	21	40	7	0.45
Permeability K (cm^2)	149	1.63E-07	1.61E-07	1.53E-07	1.05E-07	2.40E-07	1.47E-07	1.70E-07	1.36E-07	2.05E-07	2.74E-08	0.85

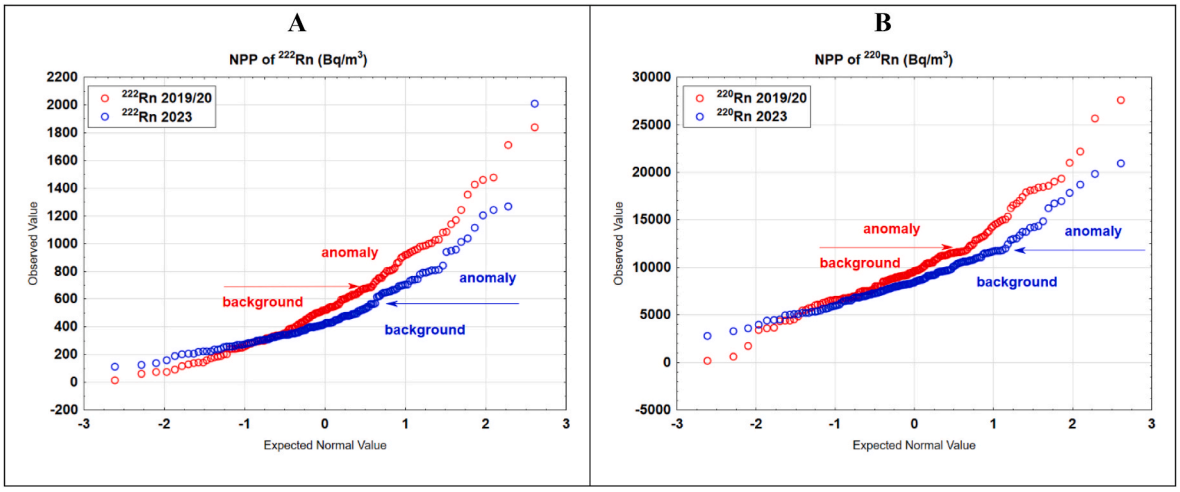

Fig. 4. Normal Probability Plots (NPP) for radon isotope concentrations. (A) NPP for ^{222}Rn and (B) NPP for ^{220}Rn, showing data from the 2019/20 campaign (red markers) and the 2023 campaign (blue markers). The inflection points in the data distribution are used to distinguish the background population from the anomalous values and to define geochemical thresholds. (For interpretation of the references to color in this figure legend, the reader is referred to the Web version of this article.)

possibly reduced emission events compared to 2019/20. A similar pattern is observed for ^{220}Rn. As concentrations increase, the data starts to deviate significantly, with the 2019/20 observations showing a more pronounced anomaly at higher values. This again indicates that ^{220}Rn concentrations were higher in 2019/20 compared to 2023, especially at the upper end of the distribution.

3.1.2. Spatial statistics

Global tests indicate that radon observations are not spatially independent. Using the 2.0 km neighbourhood distance, Global Moran's I showed significant positive spatial autocorrelation for ^{222}Rn 2023 (I = 0.085, p = 0.002), ^{222}Rn 2019/20 (I = 0.044, p = 0.006) and ^{220}Rn 2023 (I = 0.035, p = 0.012), whereas ^{220}Rn 2019/20 exhibited weaker, non-significant spatial dependence at this scale (I = 0.015, p = 0.102). Consistently, the standardised z-score of the Getis–Ord General G was negative and significant for ^{222}Rn in 2023 (z = −2.597, p = 0.006), ^{222}Rn in 2019/20 (z = −2.062, p = 0.034) and ^{220}Rn in 2023 (z = −2.479, p = 0.010), indicating a predominance of low-value clustering at the global scale, while ^{220}Rn in 2019/20 was not significant (z = −1.544, p = 0.122). FDR-corrected Gi^* maps further reveal geographically constrained hot and cold spots (Fig. S3). For ^{222}Rn in 2019/20, statistically significant cold spots occur mainly in the northern–central sector, whereas hot spots are sparse and limited to a few southern sites (Fig. S3a). In 2023, the pattern becomes more polarized, with a localized hot-spot cluster in the south-western sector and an extensive belt of cold spots spanning the central to north-eastern sector (Fig. S3b). In contrast, ^{220}Rn in 2019/20 shows no significant hot/cold spots after FDR correction (Fig. S3c), while ^{220}Rn 2023 exhibits a coherent field of cold spots in the central–eastern sector accompanied by a small, localized hot-spot area in the north-western sector (Fig. S3d). Overall, these results confirm spatial dependence in the dataset; therefore, correlations and anomaly patterns are interpreted in a spatial context and supported by spatial clustering diagnostics.

3.1.3. Spatial prediction maps

Fig. 5(A–D) shows the spatial prediction maps of ^{222}Rn and ^{220}Rn concentrations in soil gases (natural logarithmic scale) for the 2019/20 and 2023 surveys, obtained using Empirical Bayesian Kriging Regression Prediction (EBKRP) including sampling depth as an explanatory variable. Before interpreting the spatial patterns highlighted by the maps, we quantified the predictive performance of the model and the added value of including depth compared to simpler baselines. In particular, a "depth-only" baseline (Ln^{222}Rn = a + b·Depth) was evaluated using leave-one-out cross-validation (LOOCV): in 2023, this baseline reduces the error compared to a "mean-only" reference (RMSE: 0.480 → 0.425), indicating that depth captures a systematic component of ^{222}Rn variability. The EBKRP approach further improves predictive power (RMSE, 2023 = 0.400) compared to both EBK without covariates (RMSE = 0.471) and the depth-only baseline (RMSE = 0.425), supporting the adoption of EBKRP for mapping in the 2023 campaign. For the 2019/20 campaign, the effect of depth is more limited (baseline depth-only: RMSE 0.705 → 0.659), consistent with a spatial structure that is less resolvable at the sampling scale. The main cross-validation diagnostic metrics for EBK and EBKRP (including standardized statistics and mean standard error) are reported in Table S1.

In the 2019/20 survey (Fig. 5A), widespread anomalies of ^{222}Rn are observed in the NE, SW, and S zones of the study area. Small, localized anomalies are also present around Lake Fryxell and in the central area.

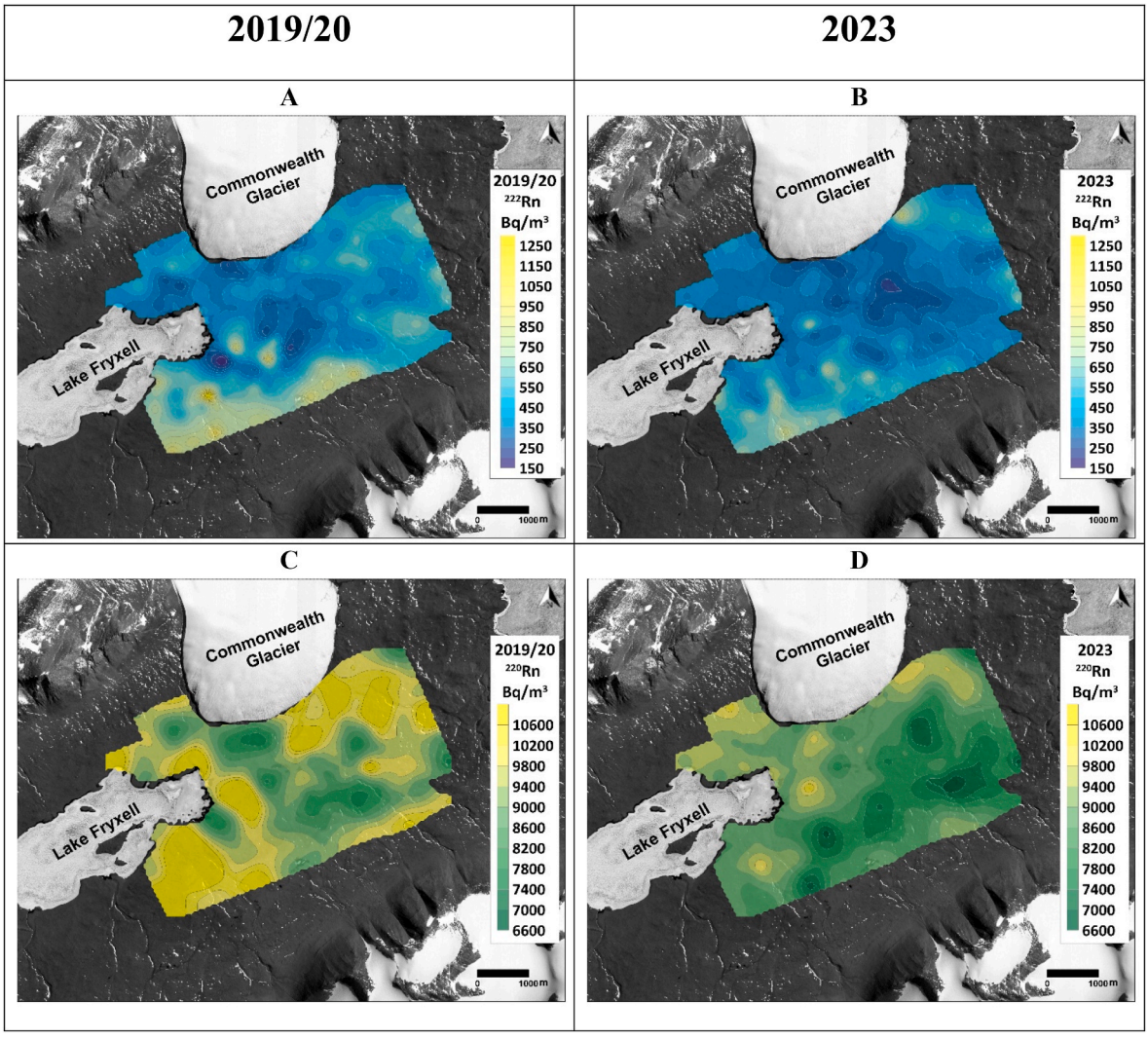

Fig. 5. Contour maps of ^{222}Rn and ^{220}Rn soil activity are shown for both 2019/20 campaign (A,C), and 2023 campaigns (B,D). The color scales used are different depending on the isotope (blue-yellow for ^{222}Rn and green-yellow for ^{220}Rn). (For interpretation of the references to color in this figure legend, the reader is referred to the Web version of this article.)

The lowest values were recorded in areas with particularly wet soil, near Lake Fryxell, south of Commonwealth Glacier, and near ponds and streams within the study area (see Fig. 1). In the 2023 campaign (Figs. 5B), ^{222}Rn soil activity shows similarities to the 2019/20 season, although the anomalies are much less widespread. They are still present in the SW, S, and NE sectors, but with lower values compared to the previous campaign. The lowest recorded values are found south of Commonwealth Glacier and in the central area, and they do not show the same correlation with wetland areas observed during the 2019/20 campaign. This suggests that the surface water circulation was more limited during the 2023 season.

As for ^{220}Rn soil activity in 2019/20 (Fig. 5C), positive anomalies are distributed in the E-NE and S-SW sectors. Notable anomalies are present around Lake Fryxell. The lowest values are found in the area southwest of Commonwealth Glacier and in the central part of the study area where particularly wet soil was observed during the 2019/20 season. The 2023 survey, shows significantly fewer ^{220}Rn anomalies (Fig. 5D), with elevated values in the NW sector and slightly anomalous values in the NE sector. The localized anomalies to the ESE of Lake Fryxell remain confirmed. The lowest values were recorded in the central area of the study site and southwest of Commonwealth Glacier, and as ^{222}Rn in 2023, they do not show a strong correlation with the surface hydrology of the valley.

The permeability (k) contour map (Fig. S4), measured only in 2023, shows higher values in the S, SW, and E of the study area, while the remaining zones show low permeability values with some localized exceptions. The limited surface water circulation during the 2023 season prevents a clear correlation between these measured permeability values and the ^{222}Rn and ^{220}Rn values measured in 2019/20. However, the map still provides an indication of the intrinsic permeability of the soil in lower Taylor Valley.

3.2. Characterization of the local radon source

Results from high-resolution γ-ray spectrometry are summarized in Table 2 (all individual data are reported in Table S2), where ^{226}Ra and ^{228}Ac activities are expressed in Bq kg^{-1} as mean, range, and standard

Table 2
Statistical summary of ^{226}Ra and ^{228}Ac activity concentrations in sediment samples collected in Taylor Valley (Antarctica). Values are reported in Bq kg^{-1} as mean, range, and standard deviation (σ).

Radionuclide	Mean and (range)	σ
^{226}Ra (Bq kg^{-1})	29.2 (12-49.9)	8.5
^{228}Ac (Bq kg^{-1})	39.8 (27.5-59.1)	6.3

deviation. These radionuclides were selected because they are the gamma-derived indicators most directly relevant to the radon dataset: ^{226}Ra constrains the source term of ^{222}Rn, whereas ^{228}Ac is used here as an indirect proxy for the ^{232} Th decay series relevant to ^{220}Rn production. The gamma-spectrometric dataset indicates moderate lateral variability of the shallow lithogenic source term across the surveyed sector (Fig. 6). The distribution of ^{226}Ra is spatially heterogeneous and patchy, with low- and intermediate-activity sites interspersed with a limited number of local enrichments, rather than defining a simple large-scale gradient across the grid (Fig. 6A). By contrast, ^{228}Ac shows a more homogeneous spatial pattern, with most samples falling within the intermediate class and only a few isolated higher-activity sites (Fig. 6B). Overall, the observed activities fall within the low-to-moderate range expected for lithogenic materials typical of Victoria Land and are broadly consistent with previous natural radioactivity data reported from the Lake Fryxell/Taylor Valley area (Komura et al., 1984; Schön, 2015; Dowling et al., 2019).

Natural radioactivity data in Antarctic terrestrial materials remain relatively scarce because of the logistical difficulty of fieldwork and the generally limited exposure of rock and soil outcrops across most of the continent. The MDV are therefore an important exception, owing to their wide and persistently deglaciated surfaces, which allow direct access to soils and sediments during the austral summer. In this context, the gamma-spectrometric dataset provides an independent constraint on the spatial variability of the shallow lithogenic source term, against which laboratory exhalation results and field soil-gas concentrations can be compared in the following sections.

3.3. Exhalation rates of ^{222}Rn and ^{220}Rn

^{222}Rn and ^{220}Rn exhalation rates of the collected soil samples (Table S3) ranged from 0.059 to 0.413 Bq/m^2 h^1 and from 397 to 1323 Bq/m^2 h^1, respectively. Seven out of 22 samples showed a low slope of the ^{222}Rn growth curve within the circuit, resulting in a negative ^{222}Rn exhalation rate within the error range, consistent with a low radon emanation rate. In contrast, all samples provided a significant average ^{220}Rn activity concentration in the experimental set-up and high exhalation rates of ^{220}Rn, due to its short half-life and rapid circulation in the apparatus.

Reference values of equilibrium radon activity concentration in soil pores (^{222}Rn eq and ^{220}Rn eq, see Table S3) were calculated from laboratory-measured radon exhalation rates at 30 °C under dry conditions using ^{222}Rn and ^{220}Rn decay constants (λ^{222} and λ^{220}, respectively) and soil porosity (n). See equations (5) and (6).

$$^{222}\text{Rn eq} = m \cdot (1 - e^{\lambda 222 \cdot 480}) / (\lambda^{222} \cdot n) \quad (5)$$

$$^{220}\text{Rn eq} = (E^{220} \cdot e^{\lambda 220 \cdot V1/Q}) / (\lambda^{220} \cdot V_0 \cdot n) \quad (6)$$

The meaning of m, E^{220}, V_1, V_0 and Q were previously defined. Porosity values were inferred from Trinh-Le (2017) based on the lithological and granulometric nature of soil samples. Samples collected in the survey of 2019/20 were used for this calculation. For the ^{222}Rn equilibrium calculation, the emanation coefficient used in the Åkerblom-type formulation ($\varepsilon = 0.28\%$) was not adopted as a generic literature value, but represents the mean site-specific coefficient derived from the 22 laboratory-characterized soil samples analysed in this study. As such, it is treated here as a first-order parameter describing the shallow source term under standardized laboratory conditions.

Calculated ^{222}Rn and ^{220}Rn equilibrium activity concentrations in soil gas were compared with in-situ soil-gas measurements from the 2019/20 and 2023 field surveys (Fig. 7A and B and Fig. 7C and D, respectively). Calculated and field values show isotope-specific behavior. For ^{220}Rn, laboratory-based equilibrium estimates generally exceed in-situ measurements, consistent with systematic underestimation during field sampling. By contrast, ^{222}Rn field values are often comparable to, or locally higher than, the production-based estimates. Laboratory determinations were standardized under dry conditions at 30 °C to ensure a comparable experimental framework; however, this standardization does not reproduce the full range of in-situ temperature and moisture conditions at the time of sampling. Higher temperature generally enhances radon release, while water content can increase radon exhalation at low values but suppress it at higher contents (Castelluccio et al., 2015). Although this standardization neglects site-specific environmental variability, the comparison remains informative because agreement (or lack thereof) between calculated and measured values provides insight into the dominant source domain and the effective transport depth of ^{222}Rn and ^{220}Rn in soil gas.

For the 2019/20 survey, no correlation was observed between calculated and measured ^{222}Rn soil-gas activity concentrations (Fig. 7A). The Pearson test, based on 11 out of 22 samples (excluding those not collected at the same place and time as soil-gas measurements and those with a negative radon exhalation value within the error range), was not significant because the correlation coefficient ($R = 0.122$) was lower than the critical correlation coefficient for the selected significance level (Rcrit = 0.419; $p = 0.20$). In contrast, calculated and measured ^{220}Rn concentrations showed a clear positive relationship for the 2019/20 campaign (Fig. 7B): 17 out of 22 samples (excluding those not collected at the same place and time as soil-gas measurements)

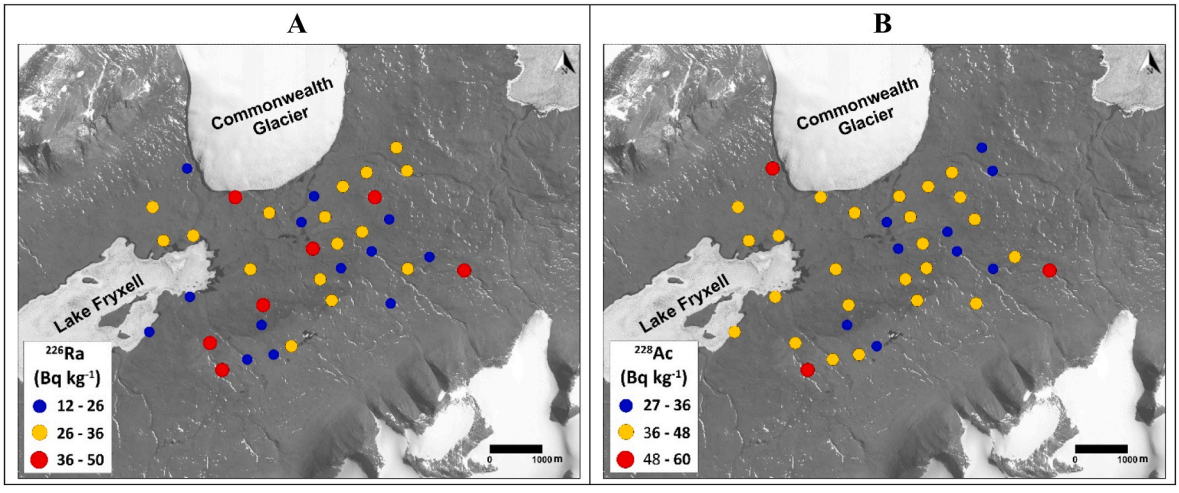

Fig. 6. Spatial distribution of gamma-derived radionuclide indicators used to constrain the shallow lithogenic source term. (A) ^{226}Ra activity in bulk sediment, relevant to ^{222}Rn production; (B) ^{228}Ac activity in bulk sediment, shown as an indirect proxy for the ^{232} Th decay series relevant to ^{220}Rn production.

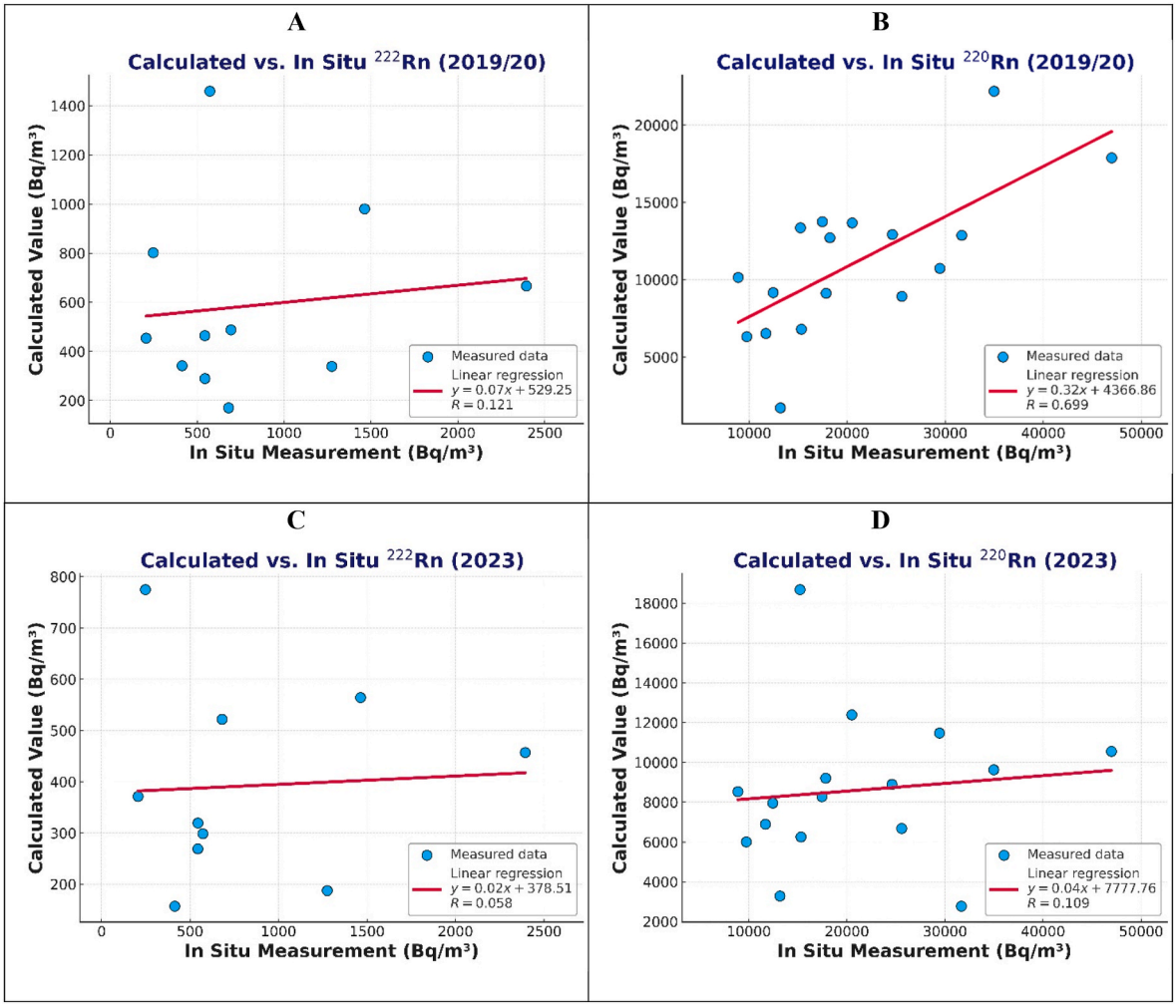

Fig. 7. Comparison between laboratory-calculated and in-situ measured ^{222}Rn and ^{220}Rn concentrations for the 2019/20 campaign. (A and B, respectively) and for the 2023 campaign (C and D).

yielded a positive correlation (R = 0.699), exceeding the critical correlation coefficient for the selected significance level (Rcrit = 0.606; p = 0.01). For the 2023 survey, no correlation was found for ^{222}Rn when using exhalation rates measured on samples collected in 2019/20, assuming the same composition (p = 0.20; Fig. 7C). The corresponding comparison for ^{220}Rn in 2023 is shown in Fig. 7D.

To further assess the relationship between expected and observed concentrations for both isotopes and both campaigns, we analysed the ratio between *in-situ* and calculated values (Table 3). The two isotopes exhibit distinct behaviours. For ^{222}Rn, the mean *in-situ*/calculated ratio was 1.12 (±1.04) in 2019/20, and 0.84 (±0.93) in 2023. Conversely, for ^{220}Rn the mean ratio remained consistently below one, with 0.58 (±0.24) in 2019/20 and 0.49 (±0.29) in 2023, indicating that *in-situ* ^{220}Rn measurements were, on average, approximately half of the calculated theoretical values.

Table 3
Descriptive statistics for the ratio of in-situ measured to theoretically calculated soil gas concentrations.

Isotope	Campaign	Mean Ratio	Std. Dev.	Range
^{222}Rn	2019/20	1.12	1.04	0.25 – 3.24
	2023	0.84	0.93	0.15 – 3.13
^{220}Rn	2019/20	0.58	0.24	0.13 – 1.14
	2023	0.49	0.29	0.09 – 1.23

3.4. Meteorological context during sampling

Sampling-day meteorological conditions differed substantially between the two campaigns. During 2019/20, mean air temperature (3 m) was −1.37 °C at EXEM and −0.53 °C at FRLM, while in 2023 it was −4.20 °C (EXEM) and −3.18 °C (FRLM). Soil temperature at 10 cm averaged 3.64–2.93 °C in 2019/20, but 0.45–0.54 °C in 2023. The higher shallow-soil temperatures relative to air temperature are consistent with strong summer solar heating of the dark, dry sediment surface in the MDV, which can produce marked thermal decoupling between the atmosphere and the upper active layer. This marked air–soil thermal decoupling is relevant because it affects the thawed state of the active layer and, consequently, the near-surface conditions controlling soil-gas transport during sampling. Mean wind speeds were comparable between campaigns (EXEM: 4.11 vs 3.90 m s^{-1}; FRLM: 4.47 vs 4.63 m s^{-1}). Barometric pressure recorded during soil-gas measurements was lower and less variable in 2023 (median 974.5 hPa; IQR 5.7) than in 2019/20 (median 983.5 hPa; IQR 11.6). These contrasts provide the environmental framework for interpreting interannual differences in soil-gas radon patterns (Fig. 8). Relative humidity (RH) was also available from the meteorological stations, but it is not shown here because RH is strongly temperature-dependent and does not directly represent soil water availability or pore-space ice in this hyper-arid polar desert setting. Accordingly, we focus on variables more directly linked to gas transport (temperature, wind speed and barometric pressure).

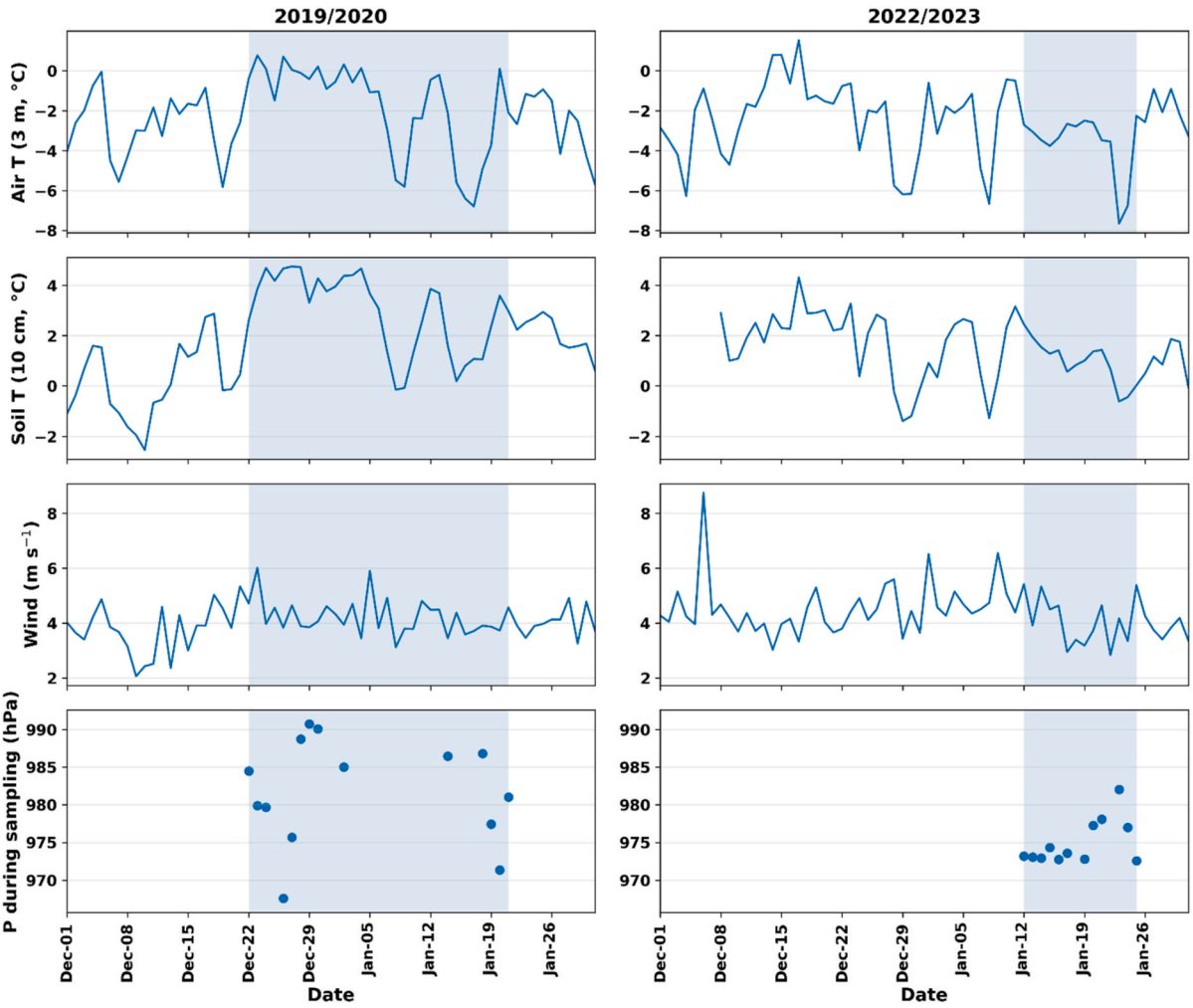

Fig. 8. Meteorological context for the two campaigns. Daily mean air temperature (3 m), soil temperature (10 cm depth) and wind speed are averaged across the EXEM and FRLM stations for 1 December–31 January in 2019/20 and 2022/23. Barometric pressure is shown as daily means computed from the pressure recorded at each soil-gas measurement on sampling days. Shaded bands indicate the sampling windows.

4. Discussion

The integrated analysis of our geochemical, laboratory, and environmental datasets from Taylor Valley provides a robust framework for interpreting permafrost dynamics in Antarctica. The central finding of our study hinges on the starkly different behaviour of the two radon isotopes, ^{222}Rn and ^{220}Rn. This isotopic decoupling, driven by their vastly different half-lives, is the key to differentiating between shallow soil processes and deeper geological gas migration. The rapid decay of ^{220}Rn restricts its migration to very short distances, making it an excellent tracer for near-surface soil properties like permeability and local ^{232}Th content. Conversely, the much longer half-life of ^{222}Rn allows it to travel significant distances from its point of origin, especially when advected by a carrier gas (e.g., CO_2, CH_4), thus making it a sensitive indicator of deeper subsurface structures and gas pathways. Integrated results strongly suggest that the largest ^{222}Rn anomalies observed in the field are difficult to reconcile with local *in-situ* production from the shallow active layer alone. This inference is based on three converging observations: (i) the shallow source term was independently constrained through gamma-derived radionuclide content and laboratory exhalation measurements, (ii) the production-based equilibrium envelope is exceeded by the strongest field values, and (iii) measurements were performed at the base of a relatively thin active layer, limiting the extent to which redistribution restricted to the thawed layer alone can generate the highest observed ^{222}Rn concentrations. This isotopic difference is also reflected in spatial patterns: ^{222}Rn tended to build consistent and repetitive anomalous domains between the two campaigns, while ^{220}Rn returned more fragmented and local signals. Such a pattern is consistent with long-range connectivity and advection affecting ^{222}Rn, while ^{220}Rn remains dominated by near-surface controls and micro-scale soil heterogeneity.

We acknowledge that advection from below the active layer is not the only process that may influence the observed ^{222}Rn distribution. Variability within the active layer itself, including differences in grain size, consolidation state, cryofacies, and local gas exchange with the atmosphere, may contribute to part of the measured signal. Sampling-induced perturbation and atmospheric dilution may also vary as a function of soil texture and near-surface permeability. These mechanisms are therefore likely to modulate local ^{222}Rn variability. However, they are less satisfactory for explaining the strongest anomalies observed in this study. The shallow source term was not treated as unconstrained, but was directly characterized through two complementary laboratory datasets: 36 sediment samples analysed for gamma-derived radionuclide content and 22 samples analysed for ^{222}Rn and ^{220}Rn exhalation. The spatial variability of ^{226}Ra and ^{228}Ac confirms that the shallow lithogenic source term is heterogeneous across the study area; however, this heterogeneity alone does not appear sufficient to account for the strongest ^{222}Rn anomalies observed in the field. Moreover, the active layer is generally thin (15–60 cm), and measurements were performed at its base, which limits the extent to which redistribution restricted to the

active layer alone can generate the highest observed ^{222}Rn concentrations. For this reason, we interpret shallow heterogeneity as a modulating factor, but not as the main process responsible for the strongest ^{222}Rn exceedances.

We found a statistically significant correlation (R = 0.699) between ^{220}Rn concentrations measured *in-situ* and the exhalation rates from corresponding soil samples analysed in the lab, confirming its shallow origin (Tuccimei et al., 2009; Castelluccio et al., 2015). For ^{222}Rn, however, no correlation emerged (R = 0.122), indicating that its presence in soil gas is governed by processes other than local production. Moreover, the comparison of *in-situ* soil gas concentrations with theoretically calculated values reveals a crucial divergence in the behaviour of ^{222}Rn and ^{220}Rn. A primary methodological factor to consider is the potential for atmospheric dilution during sampling. The process of pumping gas from a shallow depth (15-60 cm for at least 15 min) can introduce ambient air into the sample, an effect that would lead to an underestimation of *in-situ* concentrations for both isotopes. Although atmospheric mixing dilutes both isotopes, the net effect on the final measurement differs because their capacity to recover from dilution is fundamentally different: ^{220}Rn cannot be replenished during pumping because of its very short half-life, whereas ^{222}Rn can be sustained by a much larger contributing pore-gas volume and, where present, by advective supply from deeper levels. The impact of this dilution is most evident in the ^{220}Rn results. With a mean *in-situ* to calculated ratio of 0.58 in 2019/20 and 0.49 in 2023, the measured concentrations were consistently about half of the expected values. Due to its extremely short half-life, ^{220}Rn migration is limited to short distances from its point of origin. It is therefore highly susceptible to surface-level atmospheric mixing and cannot be replenished from deeper soil layers to compensate for the dilution introduced during sampling. The significant underestimation of ^{220}Rn is therefore a clear indicator of sampling-related atmospheric dilution. Given its 55.6 s half-life, ^{220}Rn cannot be replenished during pumping; accordingly, its systematic field-to-theoretical deficit (mean *in-situ*/calculated ratio 0.49–0.58) provides an internal diagnostic of this artefact. This is important because it implies that shallow sampling effects and variable atmospheric exchange can plausibly dampen or blur the field signal, but they are not sufficient to generate the highest ^{222}Rn exceedances above the local production envelope. In contrast, the ^{222}Rn ratios were 1.12 in 2019/20 and 0.84 in 2023, values that are notably close to unity and significantly higher than those for ^{220}Rn. If atmospheric dilution were the only active process, the ^{222}Rn ratio should also be substantially less than one. The fact that the measured concentration is close to, or even exceeds, the expected value, despite the dilution effect demonstrated by the ^{220}Rn data suggests that an additional source of ^{222}Rn is compensating for the loss due to atmospheric dilution. Given its longer half-life, ^{222}Rn can migrate over much wider distances. Therefore, the most likely explanation is advection of radon from a deeper source, likely from beneath the permafrost. This upward transport supplies additional ^{222}Rn to the shallow soil layer, balancing or even outweighing the concentration loss caused by atmospheric mixing during measurement. Importantly, dilution can only reduce the measured concentration; therefore, any ^{222}Rn exceedance above the local equilibrium envelope (~660–700 Bq m^{-3}) represents a conservative (minimum) estimate and cannot be explained by the sampling artefact alone.

To reduce the risk that depth-related sampling effects were misinterpreted as horizontal spatial structure, we adopted a modelling approach that separates depth-driven variability from residual spatial patterns. The improved cross-validation performance relative to simpler models (Table S1) supports the use of this approach for interpreting the mapped anomalies.

This interpretation is further supported by geochemically constrained threshold analysis. Using site-specific soil parameters, e.g., average ^{226}Ra activity of 29.58 Bq/kg, emanation coefficient of 0.28%, effective porosity (n = 21%), and soil density (ρ = 1692 kg/m^3), and applying the Åkerblom (1993) formulation, we obtained an equilibrium ^{222}Rn concentration of approximately 660 Bq/m^3. The emanation coefficient used in this calculation was derived from the laboratory dataset of the present study and represents a mean site-specific value, rather than a generic constant adopted from literature. We acknowledge that emanation depends on sediment texture, pore structure, and the effective availability of radium at grain surfaces; however, in this study these controls are incorporated into the variability of the measured sample-specific parameter sets and are therefore reflected in the uncertainty range of the resulting equilibrium estimate. This production-based estimate is statistically compatible with the anomaly threshold of ~700 Bq m^{-3} derived independently from the probability plots, and is therefore interpreted here as a physically grounded reference envelope for shallow production rather than as a fixed universal threshold. The adopted soil density is consistent with independent permafrost measurements from the MDV (Anderson et al., 2023). To strengthen the comparison between the production-based equilibrium estimate and the statistically derived anomaly threshold, we explicitly quantified uncertainty for both quantities. Using the parameter sets measured/compiled for the 22 soil samples, the resulting equilibrium estimate is 660 Bq/m^3 on average, with substantial between-sample variability (1σ = 399 Bq/m^3; CV ≈ 61%), and a 95% confidence interval for the mean of 478-841 Bq/m^3. In parallel, the anomaly threshold derived from NPP (Sinclair method) was treated as a statistical estimator and its uncertainty was evaluated by bootstrap resampling of the 2019/20 and 2023 datasets, yielding a breakpoint of 702 Bq/m^3 with a bootstrap 95% confidence interval of 588-763 Bq/m^3. The two estimates are therefore statistically compatible: their point values differ by ~6-7%, and the threshold lies well within the uncertainty bounds of the production-based equilibrium constraint (and vice versa). This supports the interpretation that exceedances above ~700 Bq/m^3 are not an artefact of distribution skewness, but correspond to concentrations that are difficult to reconcile with shallow *in-situ* production alone, consistent with an additional advective contribution from depth.

The spatial distribution of these anomalies provides insight into the likely transport pathways of ^{222}Rn. Contour maps show that elevated ^{222}Rn concentrations are not randomly distributed but recur in specific sectors (Fig. 9A and B), notably in the SW and S areas during both the 2019/20 and 2023 campaigns. This spatial persistence is consistent with relatively stable, site-specific controls on gas transport, including preferentially more permeable and/or fractured zones at the base of the active layer and immediately beneath it within the shallow frozen substrate.

Interestingly, although the overall geometry of the anomalous domains remains similar between campaigns, their spatial distribution and intensity are reduced in 2023. This pattern is consistent with a decrease in transport efficiency between campaigns, likely to be related to changes in active-layer permeability and near-surface gas connectivity. Differences in active-layer thickness and continuity, as well as ice-related tortuosity, can plausibly reduce effective gas transport and dampen the surface expression of long-lived ^{222}Rn. Consequently, these pathways may remain spatially stable, while their capacity for upward ventilation varies seasonally with thermal and hydrological conditions. These anomalous zones also tend to coincide with measurements displaying higher ^{222}Rn/^{220}Rn ratios (red dots). In principle, because short-lived ^{220}Rn decays rapidly, elevated ^{222}Rn/^{220}Rn may reflect a longer effective transport distance and/or reduced contribution from near-surface production. However, since ^{220}Rn is systematically underestimated due to atmospheric dilution during sampling, the ^{222}Rn/^{220}Rn metric should be treated as a qualitative indicator rather than a definitive “depth fingerprint”. Accordingly, we use ^{222}Rn/^{220}Rn only as supporting evidence, and we focus on zones where elevated ratios co-occur with ^{222}Rn concentrations exceeding the anomaly threshold. Furthermore, the spatial distribution of anomalous zones highlighted by ^{222}Rn and by the ^{222}Rn/^{220}Rn ratio overlap with multi-gas anomalous areas previously reported for CO_2, CH_4, CO_2 flux, He and H_2 (Ruggiero et al., 2023). This comparison is informative because advective transport

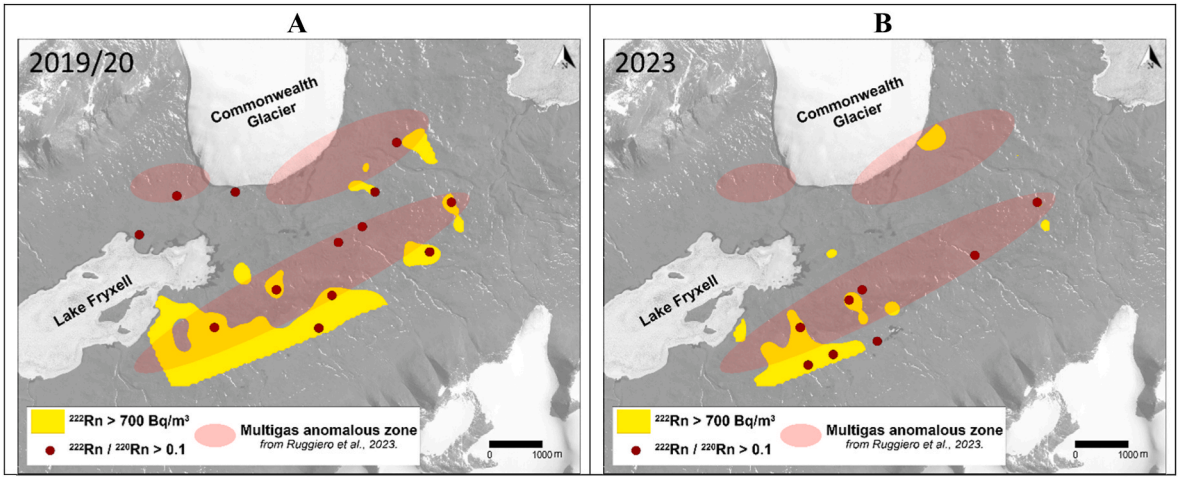

Fig. 9. The map shows yellow areas where ^{222}Rn concentrations exceeded the 700 Bq/m^3 anomaly threshold and, in red dots, where the ^{222}Rn/^{220}Rn ratio is greater than 0.1, during the 2019/20 campaign (A) and the 2023 campaign (B). These areas are superimposed on the multigas anomalous zones identified by Ruggiero et al. (2023) (pink shaded areas). (For interpretation of the references to color in this figure legend, the reader is referred to the Web version of this article.)

associated with CO_2 and CH_4 can act as carrier mechanism, enhancing upward migration of ^{222}Rn. Taken together, these converging observations support the interpretation that preferential permeability structures (e.g., fractures and fault-related damage zones) may channel gas transport, with their effectiveness potentially modulated by seasonal freeze–thaw processes within the active layer.

The reduced intensity and spatial extent of ^{222}Rn anomalies observed in 2023 is consistent with combined thermal and atmospheric control on soil–gas transport (Fig. 8). Colder air and soil temperatures during the 2023 sampling period reduced the thickness and/or permeability of the seasonally active layer, while increasing ice-related tortuosity, thereby shortening the effective transport distance of long-lived ^{222}Rn. In addition, the 2019/20 campaign shows a weak-to-moderate inverse association between ^{222}Rn and barometric pressure, consistent with episodic pressure-driven ventilation ("barometric pumping") that can transiently enhance soil–gas release in dry, porous media. Wind speed did not show a consistent relationship with ^{222}Rn across campaigns, suggesting that pressure variability and thermal state may dominate short-term modulation in this setting. Overall, the interannual contrast highlights that soil-gas radon signals integrate both source strength and transport efficiency, the latter being sensitive to meteorological conditions on timescales of days to weeks. Since our comparison is based on two field seasons, attribution remains provisional; additional multi-year surveys coupled with direct active-layer state measurements are required to quantify causality. Beyond local geological interpretation, delineating persistent zones of high subsurface connectivity is environmentally relevant because the same pathways that facilitate ^{222}Rn transport can also promote upward migration of co-occurring gases (e.g., CO_2 and CH_4) and other geogenic constituents. Using probability-based anomaly thresholds anchored to site-specific production constraints provides a transparent basis for separating transport-driven exceedances from locally produced background, improving comparability across campaigns and regions. Although thaw-related changes in permeability are inferred here indirectly, the interannual differences motivate integrated monitoring that couples measurements of radon isotopes with subsurface temperature and moisture, as well as atmospheric forcing. More broadly, radon-isotope mapping offers a scalable tool for environmental surveillance of permafrost integrity, helping prioritize sites for intensified measurements and tracking the emergence or reactivation of ventilation corridors as polar climates warm.

5. Conclusions

By combining repeated, valley-scale soil-gas surveys with laboratory constraints on radon/thoron production, this study shows that ^{222}Rn and ^{220}Rn provide complementary information on Antarctic permafrost dynamics in Taylor Valley.

^{220}Rn primarily behaves as a near-surface tracer: its strong agreement with laboratory exhalation rates supports an origin within the active layer and highlights the influence of shallow soil properties (e.g., permeability and local Th-bearing substrates). By contrast, field ^{222}Rn does not correlate with production-based expectations. Moreover, measured concentrations locally approach or exceed the shallow equilibrium reference despite sampling-related dilution, which is consistent with additional replenishment by advection from beneath the active layer. A physically based equilibrium estimate (~660 Bq m^{-3}) closely matches the statistical anomaly threshold (~700 Bq m^{-3}), providing a practical criterion for identifying transport-driven ^{222}Rn exceedances.

The lower frequency and reduced spatial extent of ^{222}Rn anomalies in 2023 compared with 2019/20 suggest that short-term meteorological variability can modulate active-layer connectivity and, consequently, the efficiency of deep-gas pathways. Because ^{220}Rn is systematically underestimated during field sampling, any depth inference based on ^{222}Rn/^{220}Rn should be treated as qualitative unless future work adopts improved thoron sampling protocols and quantifies dilution effects more explicitly.

Overall, our results outline a transferable, field-practical framework for monitoring permafrost integrity in polar deserts using radon isotopes. Future efforts should couple radon isotopes with continuous subsurface temperature/moisture measurements and multi-gas observations to quantify mechanisms linking climate forcing, permeability changes, and geogenic gas emissions.

CRediT authorship contribution statement

L. Ruggiero: Writing – review & editing, Writing – original draft, Visualization, Validation, Supervision, Resources, Project administration, Methodology, Investigation, Funding acquisition, Formal analysis, Data curation, Conceptualization. **A. Sciarra:** Writing – review & editing, Supervision, Methodology, Investigation, Formal analysis, Data curation, Conceptualization. **A. Mazzini:** Writing – review & editing, Investigation. **F. Florindo:** Writing – review & editing, Investigation. **G. Wilson:** Writing – review & editing, Supervision, Investigation. **C. Mazzoli:** Writing – review & editing, Investigation. **P. Tuccimei:** Writing – review & editing, Writing – original draft, Visualization, Methodology. **G. Galli:** Writing – review & editing, Methodology, Investigation, Data curation. **L. Tositti:** Writing – review & editing, Writing – original draft, Visualization, Methodology. **A. Zappi:** Writing

– review & editing, Investigation. **J. Anderson:** Writing – review & editing, Investigation. **L. Davidson:** Writing – review & editing, Investigation. **E. Benà:** Writing – review & editing, Investigation. **V. Olivetti:** Writing – review & editing, Investigation. **M.C. Tartarello:** Writing – review & editing, Investigation. **M. Mattia:** Writing – review & editing, Investigation. **F. Giagnoni:** Writing – review & editing, Investigation. **C. Zaccone:** Writing – review & editing. **S. Bigi:** Writing – review & editing, Resources. **R. Sassi:** Writing – review & editing, Investigation. **G. Ciotoli:** Writing – review & editing, Validation, Methodology, Formal analysis, Data curation, Conceptualization.

Funding

This work was funded by the Ministero dell'Istruzione dell'Università e della Ricerca through PNRA 2018 n° 00253 linea D, prot.73633/2019 (SENECA PROJECT: Source and origin of greenhouse gases in Antarctica).

Declaration of competing interest

The authors declare that they have no known competing financial interests or personal relationships that could have appeared to influence the work reported in this paper.

Acknowledgments

All data were collected within the framework of the PNRA SENECA project during the XXXV and XXXVIII Italian expeditions to Antarctica. We acknowledge UTA-ENEA and Antarctica New Zealand for providing logistical and technical support, and the personnel at Scott Base for hosting our team. We also wish to thank Dr. Irene Stefanelli for calibrating the device employed for soil permeability measurements. The authors sincerely thank the Editor and the anonymous Reviewers for their constructive comments and valuable suggestions, which helped improve the quality and clarity of this manuscript.

Appendix A. Supplementary data

Supplementary data to this article can be found online at https://doi.org/10.1016/j.envres.2026.124523.

Data availability

The datasets generated and/or analysed during the current study are available from the corresponding author on reasonable request. Meteorological data are openly available through the Environmental Data Initiative (https://doi.org/10.6073/pasta/151ac2f6bbb63a4f7c10f205f953fb46; https://doi.org/10.6073/pasta/12c8b7dff536c07ee61ccbc65a4154f8).

References

Åkerblom, G., 1993. Ground Radon: Monitoring Procedure in Sweden: Lecture at the "JAG" Disc. Meeting on "Radon Workshop, Geol., Env. Techn.", Royal Astron. Soc., London, 12 February.

Anderson, J.T.H., Fujioka, T., Fink, D., Hidy, A.J., Wilson, G.S., Wilcken, K., Abramov, A., Demidov, N., 2023. Antarctic permafrost processes and antiphase dynamics of cold-based glaciers in the McMurdo Dry Valleys inferred from 10Be and 26Al cosmogenic nuclides. Cryosphere 17, 4917–4936. https://doi.org/10.5194/tc-17-4917-2023.

Benà, E., Ciotoli, G., Ruggiero, L., Coletti, C., Bossew, P., Massironi, M., Mazzoli, C., Mair, V., Morelli, C., Galgaro, A., Morozzi, P., Tositti, L., Sassi, R., 2022. Evaluation of tectonically enhanced radon in fault zones by quantification of the radon activity index. Sci. Rep. 12, 21586. https://doi.org/10.1038/s41598-022-26124-y.

Bockheim, J.G., Campbell, I.B., McLeod, M., 2007. Permafrost distribution and active-layer depths in the McMurdo Dry Valleys, Antarctica. Permafr. Periglac. Process. 18 (3), 217–227. https://doi.org/10.1002/ppp.588.

Carshalton, A.G., Balks, M.R., O'Neill, T.A., Bryan, K.R., Seybold, C.A., 2022. Climatic influences on active layer depth between 2000 and 2018 in the McMurdo Dry Valleys, Ross Sea Region, Antarctica. Geoderma Reg. 29, e00497.

Castelluccio, M., De Simone, G., Lucchetti, C., Moroni, M., Salvati, F., Tuccimei, P., 2015. A new technique to measure *in situ* soil gas permeability. J. Geochem. Explor. 148, 56–59. https://doi.org/10.1016/j.gexplo.2014.08.002.

Cinelli, G., Tositti, L., Capaccioni, B., Brattich, E., Mostacci, D., 2015. Soil gas radon assessment and development of a radon risk map in Bolsena, Central Italy. Environ. Geochem. Health 37 (2), 305–319. https://doi.org/10.1007/s10653-014-9649-9.

Ciotoli, G., Etiope, G., Guerra, M., Lombardi, S., 1999. The detection of concealed faults in the Ofanto basin using the correlation between soil gas fracture surveys. Tectonophysics 299 (3–4), 321–332.

Ciotoli, G., Sciarra, A., Ruggiero, L., Annunziatellis, A., Bigi, S., 2016. Soil gas geochemical behaviour across buried and exposed faults during the 24 August 2016 central Italy earthquake. Ann. Geophys. 59. https://doi.org/10.4401/ag-7242.

Coletti, C., Ciotoli, G., Benà, E., Brattich, E., Cinelli, G., Galgaro, A., Massironi, M., Mazzoli, C., Mostacci, D., Morozzi, P., Mozzi, P., Nava, J., Ruggiero, L., Sciarra, A., Tositti, L., Sassi, R., 2022. The assessment of local geological factors for the construction of a Geogenic Radon Potential map using regression kriging. A case study from the Euganean Hills volcanic district (Italy). Sci. Total Environ. 808, 152064. https://doi.org/10.1016/j.scitotenv.2021.152064.

Cressie, N., 1993. Statistics for Spatial Data, revised ed. Wiley, New York, p. 900.

De Risi, R., De, Luca F., EL Gilder, C., Pokhrel, R.M., Vardanega, J.P., 2021. The SAFER geodatabase for the Kathmandu valley: bayesian kriging for data-scarce regions. Earthq. Spectra 37 (2), 1108–1126. https://doi.org/10.1177/8755293020970977.

Dowling, C.B., Welch, S.A., Lyons, W.B., 2019. The geochemistry of glacial deposits in Taylor Valley, Antarctica: comparison to upper continental crustal abundances. Appl. Geochem. 107, 91–104. https://doi.org/10.1016/j.apgeochem.2019.05.006.

Dugan, H.A., Doran, P.T., Fountain, A.G., 2025a. High-frequency, hourly, and daily measurements from Explorers Cove Meteorological Station (EXEM). Mcmurdo Dry Valleys, Antarctica (1997-2025, Ongoing) Ver 20. Environmental Data Initiative. https://doi.org/10.6073/pasta/151ac2f6bbb63a4f7c10f205f953fb46.

Dugan, H.A., Doran, P.T., Fountain, A.G., 2025b. High-frequency, hourly, and daily measurements from Lake Fryxell Meteorological Station (FRLM). Mcmurdo Dry Valleys, Antarctica (1993-2025, Ongoing) Ver 19. Environmental Data Initiative. https://doi.org/10.6073/pasta/12c8b7dff536c07ee61ccbc65a4154f8.

Etiope, G., Lombardi, S., 1995. Evidence for radon transport by carrier gas through faulted clays in Italy. J. Radioanal. Nucl. Chem. 193 (2), 291–300.

Etiope, G., Martinelli, G., 2002. Migration of carrier and trace gases in the geosphere: an overview. Phys. Earth Planet. Inter. 129 (3–4), 185–204. https://doi.org/10.1016/S0031-9201(01)00292-8.

Foley, N., Tulaczyk, S.M., Grombacher, D., Doran, P.T., Mikucki, J., Myers, K.F., et al., 2019. Evidence for pathways of concentrated submarine groundwater discharge in East Antarctica from helicopter-borne electrical resistivity measurements. Hydrology 6 (2), 54. https://doi.org/10.3390/hydrology6020054.

Fountain, A.G., Nylen, T.H., Monaghan, A., Basagic, H.J., Bromwich, D., 2010. Snow in the McMurdo dry valleys, Antarctica. Int. J. Climatol.: A Journal of the Royal Meteorological Society 30 (5), 633–642.

Garland, J.A., Cambray, R.S., Johnson, C.E., 1993. Atmospheric radioactivity and its variations. In: Hewitt, C.N., Sturges, W.T. (Eds.), Global Atmospheric Chemical Change. Springer, Dordrecht. https://doi.org/10.1007/978-94-011-1864-4_9.

Gilmore, G., Joss, D., 2024. Practical gamma-ray Spectrometry. John Wiley & Sons.

Giustini, F., Ciotoli, G., Rinaldini, A., Ruggiero, L., Voltaggio, M., 2019. Mapping the geogenic radon potential and radon risk by using empirical Bayesian Kriging regression: a case study from a volcanic area of central Italy. Sci. Total Environ. 661, 449–464. https://doi.org/10.1016/j.scitotenv.2019.01.146.

Giustini, F., Ruggiero, L., Sciarra, A., Beaubien, S.E., Graziani, S., Galli, G., Pizzino, L., Tartarello, M.C., Lucchetti, C., Sirianni, P., Tuccimei, P., Voltaggio, M., Bigi, S., Ciotoli, G., 2022. Radon hazard in central Italy: Comparison among areas with different Geogenic Radon potential. Int. J. Environ. Res. Publ. Health 19 (2), 666. https://doi.org/10.3390/ijerph19020666.

Glover, P.W.J., Blouin, M., 2022. Increased radon exposure from thawing of permafrost due to climate change. Earths Future 10. https://doi.org/10.1029/2021EF002598.

Hall, B.L., Denton, G.H., 2000. Radiocarbon chronology of Ross Sea drift, eastern Taylor Valley, Antarctica: evidence for a grounded ice sheet in the Ross Sea at the last glacial maximum. Geogr. Ann. Phys. Geogr. 82 (2–3), 305–336.

Hengl, T., Heuvelink, G.B.M., Rossiter, D.G., 2007. About regression-kriging: from equations to case studies. Comput. Geosci. 33 (10), 1301–1315. https://doi.org/10.1016/j.cageo.2007.05.001.

Huxol, S., Brennwald, M.S., Henneberger, R., Kipfer, R., 2013. 220/222Rn isotope as anatural proxy for soil gas transport. Environ. Sci. Technol. 47. https://doi.org/10.1021/es4026529, 14044e14050.

King, C.Y., King, B.S., Evans, W.C., Zhang, W., 1996. Spatial radon anomalies on active faults in California. Appl. Geochem. 11 (4), 497–510.

Klimshin, A.V., Kozlova, I.A., Rybakov, E.N., Lukovskoy, M.Yu, 2010. Effect of freezing the surface layer of soil on radon transport. Vestnik KRAUNC. Earth Sci. 16 (2), 146–151.

Komura, K., Torii, T., Yamamoto, M., Sakanoue, M., 1984. Natural and artificial radionuclides in environmental samples collected from the McMurdo Sound region in South Victoria Land, Antarctica. Mem. Natl. Inst. Polar Res. - Special Issue 33, 224–236.

Kristiansson, K., Malmqvist, L., 1982. Evidence for nondiffusive transport of 86 Rn in the ground and a new physical model for the transport. Geophysics 47 (10), 1444–1452.

Krivoruchko, K., 2012. Empirical Bayesian kriging. Arcuser Fall.

Krivoruchko, K., Gribov, A., 2019. Evaluation of empirical Bayesian kriging. Spatial Statistics 32, 100368. https://doi.org/10.1016/j.spasta.2019.100368.

Leshukov, T., Legoshchin, K., Avdeev, K., Baranova, E., Larionov, A., 2024. Depth gradient and radon activity concentration in soil gas in the Zone of a potentially active fault. Earth 5 (4), 1005–1022. https://doi.org/10.3390/earth5040052.

Lucchetti, C., Briganti, A., Castelluccio, M., Galli, G., Santilli, S., Soligo, M., Tuccimei, P., 2019. Integrating radon and thoron flux data with gamma radiation mapping in radon-prone areas. The case of volcanic outcrops in a highly-urbanized city (Roma, Italy). J. Environ. Radioact. 202, 41–50. https://doi.org/10.1016/j.jenvrad.2019.02.004.

Mao, Y., Zhang, L., Wang, H., Guo, Q., 2023. The temporal variation of Radon concentration at different depths of soil: a case Study in Beijing. J. Environ. Radioact. 264, 107200.

McGinnis, L.D., Jensen, T.E., 1971. Permafrost-hydrogeologic regimen in two ice-free valleys, Antarctica, from electrical depth sounding. Quaternary Research 1, 389–409. https://doi.org/10.1016/0033-5894(71)90073-1.

McGinnis, L.D., Stuckless, J.S., Osby, D.R., Kyle, P.R., 1981. Gamma Ray, Salinity, and Electric Logs of DVDP Boreholes. American Geophysical Union (AGU), pp. 95–108.

Mikucki, J.A., Auken, E., Tulaczyk, S., Virginia, R.A., Schamper, C., Sørensen, K.I., et al., 2015. Deep groundwater and potential subsurface habitats beneath an Antarctic dry valley. Nat. Commun. 6 (1), 6831. https://doi.org/10.1038/ncomms7831.

Mollo, S., Moschini, P., Galli, G., Tuccimei, P., Lucchetti, C., Iezzi, G., Scarlato, P., 2021. Carrier and dilution effects of CO2 on thoron emissions from a zeolitized tuff exposed to subvolcanic temperatures. R. Soc. Open Sci. 8 (2), 201539.

Monaghan, A.J., Bromwich, D.H., Powers, J.G., Manning, K.W., 2005. The climate of the McMurdo, Antarctica, region as represented by one year of forecasts from the Antarctic Mesoscale Prediction System. J. Clim. 18 (8), 1174–1189.

Nazaroff, W.W., 1992. Radon transport from soil to air. Rev. Geophys. 30, 137–160.

Nazaroff, W.W., Nero Jr, A.V., 1987. Radon and its Decay Products in Indoor Air. Wiley, New York.

ORTEC, 2003. Gamma-vision 32 A66-B32 user's manual. ORTEC USA, Part No. 783620 Manual Revision D.

Pilz, J., Spöck, G., 2008. Why do we need and how should we implement Bayesian kriging methods. Stoch. Environ. Res. Risk Assess. 22, 621–632.

Puchkov, A.V., Yakovlev, E.Yu, Hasson, N.R., Sobrinho, G.A.N., Tsykareva, Y.V., 2021. Radon hazard in permafrost conditions: current state of research. Geography, Environment, Sustainability 14 (4), 93–104. https://doi.org/10.24057/2071-9388-2021-037.

Puzzilli, L.M., Ruscito, V., Madonna, S., Gentili, F., Ruggiero, L., Ciotoli, G., Nisio, S., 2024. Natural sinkhole monitoring and characterization: the case of Latera sinkhole (Latium, central Italy). Geosciences 14 (1), 18. https://doi.org/10.3390/geosciences14010018.

Romano, V., Fischanger, F., Wilson, G., Sciarra, A., Mazzini, A., Mazzoli, C., et al., 2024. Permafrost hydrogeology of Taylor Valley, Antarctica: insights from deep electrical resistivity tomography. Geophys. Res. Lett. 51 (18). https://doi.org/10.1029/2023GL106912.

Ruggiero, L., Sciarra, A., Mazzini, A., Florindo, F., Wilson, G., Tartarello, M.C., et al., 2023. Antarctic permafrost degassing in Taylor Valley by extensive soil gas investigation. Sci. Total Environ. 866. https://doi.org/10.1016/j.scitotenv.2022.161345.

Samet, J.M., 1989. Radon and lung cancer. JNCI: Journal of the National Cancer Institute 81 (10), 745–758.

Samsonova, V.P., Blagoveshchenskii, Y.N., Meshalkina, Y.L., 2017. Use of empirical Bayesian kriging for revealing heterogeneities in the distribution of organic carbon on agricultural lands. Eurasian Soil Sc 50, 305–311. https://doi.org/10.1134/S1064229317030103.

Schön, J.H., 2015. Nuclear/Radioactive properties. Dev. Petr. Sci. 65, 119–166. https://doi.org/10.1016/B978-0-08-100404-3.00005-6. Elsevier.

Sciarra, A., Mazzini, A., Inguaggiato, S., Vita, F., Lupi, M., Hadi, S., 2018. Radon and carbon gas anomalies along the Watukosek Fault System and lusi mud eruption, Indonesia. Mar. Petrol. Geol. 90, 77–90. https://doi.org/10.1016/j.marpetgeo.2017.09.031.

Sellmann, P.V., Delaney, A.J., 1990. Radon measurements as indicators of permafrost distribution. Cold Reg. Sci. Technol. 18 (3), 331–336. https://doi.org/10.1016/0165-232X(90)90029-V.

Sethi, T.K., El-Ghamry, M.N., Kloecker, G.H., 2012. Radon and lung cancer. Clin. Adv. Hematol. Oncol. 10 (3), 157–164.

Shweikani, R., Giaddui, T.G., Durrani, S.A., 1995. The effect of soil parameters on the Radon concentration values in the environment. Radiat. Meas. 25, 581–584.

Sinclair, A.J., 1991. A fundamental approach to threshold estimation in exploration geochemistry: probability plots revisited. J. Geochem. Explor. 41, 1–22.

Smetanová, I., Holý, K., Müllerová, M., Polášková, A., 2010. The effect of meteorological parameters on Radon concentration in borehole air and water. J. Radioanal. Nucl. Chem. 283, 101–109.

Stefanelli, I., 2021. Calibrazione di un dispositivo per la misura della permeabilità intrinseca da utilizzare in Antartide. In: Bachelor Degree, vol. 3. University, Roma.

Swanger, K.M., Marchant, D.R., Kowalewski, D.E., Head III, J.W., 2010. Viscous flow lobes in central Taylor Valley, Antarctica: origin as remnant buried glacial ice. Geomorphology 120 (3–4), 174–185.

Tositti, L., Pereira, E.B., Sandrini, S., Capra, D., Tubertini, O., Bettoli, M.G., 2002. Assessment of summer trends of tropospheric Radon isotopes in a coastal antarctic station (Terra Nova Bay). Int. J. Environ. Anal. Chem. 82 (5), 259–274. https://doi.org/10.1080/03067310290027767.

Tositti, L., Cinelli, G., Brattich, E., Galgaro, A., Mostacci, D., Mazzoli, C., Massironi, M., Sassi, R., 2017. Assessment of lithogenic radioactivity in the Euganean Hills magmatic district (NE Italy). J. Environ. Radioact. 166, 259–269. https://doi.org/10.1016/j.jenvrad.2016.07.01.

Tositti, L., Moroni, B., Dinelli, E., Morozzi, P., Brattich, E., Sebastiani, B., Petroselli, C., Crocchianti, S., Selvaggi, R., Goretti, E., Cappelletti, D., 2020. Deposition processes over complex topographies: experimental data meets atmospheric modeling. Sci. Total Environ. 744, 140974. https://doi.org/10.1016/j.scitotenv.2020.140974.

Toutain, J.P., Baubron, J.C., 1999. Gas geochemistry and seismotectonics: a review. Tectonophysics 304, 1–27.

Trinh-Le, C.A., 2017. Dry sedimentation processes in the high-elevation McMurdo dry Valleys. Antarctica: a Case Study in University Valley (Doctoral Dissertation. Open Access Te Herenga Waka-Victoria University of Wellington).

Tuccimei, P., Moroni, M., Norcia, D., 2006. Simultaneous determination of 222Rn and 220Rn exhalation rates from building materials used in Central Italy with accumulation chambers and a continuous solid state alpha detector: influence of particle size, humidity and precursors concentration. Appl. Radiat. Isot. 64 (2), 254–263.

Tuccimei, P., Castelluccio, M., Soligo, M., Moroni, M., 2009. Radon exhalation rates of building materials: experimental, analytical protocol and classification criteria. Building materials: Properties, performance and applications 259–274.

Vaupotič, J., Gregorič, A., Kobal, I., Žvab, P., Kozak, K., Mazur, J., Kochowska, E., Grządziel, D., 2010. Radon concentration in soil gas and radon exhalation rate at the Ravne Fault in NW Slovenia. Nat. Hazards Earth Syst. Sci. 10, 895–899. https://doi.org/10.5194/nhess-10-895-2010.

Walia, V., Su, T.C., Fu, C.C., Yang, T.F., 2005. Spatial variations of radon and helium concentration in soil-gas across the Shan-Chiao fault, Northern Taiwan. Rad. Meas. 40, 513–516. https://doi.org/10.1016/j.radmeas.2005.04.011.

Yang, T.F., Walia, V., Chyi, L.L., Fu, C.C., Chen, C.H., Liu, T.K., Song, S.R., Lee, C.Y., Lee, M., 2005. Variations of soil radon and thoron concentrations in a fault zone and prospective earthquakes in SW Taiwan. Rad. Meas 40, 496–502. https://doi.org/10.1016/j.radmeas.2005.05.017.

Yang, J., Busen, H., Scherb, H., Hürkamp, K., Guo, Q., Tschiersch, J., 2019. Modeling of radon exhalation from soil influenced by environmental parameters. Sci. Total Environ. 656, 1304–1311.

Yuce, G., Ugurluoglu, Y.D., Nadar, N., Yalcin, H.T., Yaltirak, C., Streil, T., Oeser, V., 2010. Monitoring of earthquake precursors by multi-parameter stations in Eskisehir Region (Turkey). Appl. Geochem. 25 (4), 572–579. https://doi.org/10.1016/j.apgeochem.2010.01.013.

Yuce, G., Fu, C.C., D'Alessandro, W., Gulbay, A.H., Lai, C.W., Bellomo, S., Yang, T.F., Italiano, F., Walia, V., 2017. Geochemical characteristics of soil radon and carbon dioxide within the dead sea fault and karasu fault in the amik basin (Hatay). Turkey. Chem. Geol. https://doi.org/10.1016/j.chemgeo.2017.01.003.

Zhang, S., Jin, D., Jin, H., Li, C., Hu, Y., 2024. Potential radon risk in permafrost regions of the Northern Hemisphere under climate change: a review. Earth Sci. Rev. https://doi.org/10.1016/j.earscirev.2023.104684.